minerals

MDPI

Article

The Role of Continental Crust in the Formation of Uraninite-Based Ore Deposits

Stefanie R. Lewis [1,*], Antonio Simonetti [1], Loretta Corcoran [1], Stefanie S. Simonetti [1], Corinne Dorais [1] and Peter C. Burns [1,2]

[1] Department of Civil and Environmental Engineering and Earth Sciences, University of Notre Dame, Notre Dame, IN 46556, USA; Antonio.Simonetti.3@nd.edu (A.S.); lcorcora@nd.edu (L.C.); Stefanie.Simonetti.4@nd.edu (S.S.S.); Dorais1@llnl.gov (C.D.); pburns@nd.edu (P.C.B.)

[2] Department of Chemistry and Biochemistry, University of Notre Dame, Notre Dame, IN 46556, USA

* Correspondence: stefanie.lewis08@gmail.com

Received: 19 December 2019; Accepted: 3 February 2020; Published: 6 February 2020

Abstract: This study reports trace element abundances and Pb, Sr, and U isotopic signatures of uraninite from a variety of ore deposits in order to establish baseline forensic information for source attribution of raw, natural U-rich samples. Trace element concentrations, reported here, provide insights into uraninite crystal substitution mechanisms and possible crustal sources of U, including mobility of trace elements between pristine versus altered fractions. Spatially resolved laser ablation (LA) multicollector (MC) inductively coupled plasma mass spectrometry (ICP-MS) analyses were used to determine secondary ^{207}Pb-^{206}Pb isochron ages, and these were validated by corroborative results obtained by solution mode (SM) MC-ICP-MS for the same sample. Secondary Pb-Pb isochron ages obtained, in this study, indicate that uraninite alteration occurs shortly after ore mineralization. Initial $^{87}Sr/^{86}Sr$ values correlate in general with host craton age, and therefore suggest that uraninite ore formation is closely linked to the nature of the bedrock geology. The $\delta^{238}U$ values are explained by invoking multiple physicochemical conditions and parameters such as temperature, nuclear field shift, oxidation, and source rock composition. The $\delta^{234}U$ values indicate that the uraninites, investigated here, have undergone recent alteration, but the latter has not perturbed the Pb-Pb secondary isochron ages.

Keywords: uraninite; nuclear forensics; laser ablation; inductively coupled plasma mass spectrometry; trace elements; secondary Pb-Pb isochron; Pb isotopes; Sr isotopes; U isotopes

1. Introduction

Uranium deposits of economic interest are located on most continents and are classified according to their host rock lithology, nearby tectonic structures, and mode of alteration [1]. The physicochemical conditions prevailing during U ore formation are complex and evolve continuously with time as evidenced by the occurrence of several generations of uraninite within one deposit (e.g., [2]), which is the main constituent mineral. Trace and major element incorporation by uraninite (UO_{2+x}) is extremely complex and results in a diverse chemical composition; thus, a more representative formula is $(U^{4+}_{1-x-y-z-u}U^{6+}_{x}REE^{3+}_{y}M^{2+}_{z}\square^{4-}_{u})O_{2+x-0.5y-z-2u}$, where M are divalent metal ions and □ represents a vacancy [3]. Uraninite has been the focus of numerous past investigations to understand its variable chemical nature, and because it is the most important raw material used for the production of fuel destined for nuclear reactors.

Natural uranium has three main isotopes, ^{234}U, ^{235}U, and ^{238}U, of which only ^{235}U is fissile. The latter feature of uranium has prompted the illicit trafficking of this material for the past several decades, in particular subsequent to the demise of the former Soviet Union [4]. In efforts to combat

illegal trafficking of nuclear materials, characteristic chemical and isotopic signatures have been established to help identify the origin of intercepted material. In the past, nuclear forensic signatures have been based on major and trace element concentrations, isotopic ratios (Pb, Sr, U), and morphological differences. Trace element signatures have proven effective for deposit type and provenance identification (e.g., [5,6]). Isotopic tracers employed for uraninite, such as those of U, Pb, and Sr, reported here, provide information about a material's age, origin, and possible processing enrichment history. In recent years, improvements in analytical methods and equipment have enhanced the reporting of chemical and isotopic signatures at faster time scales and with lower detection limits (e.g., [7,8]). Consequently, there has been renewed interest and more detailed investigations into the U isotope signatures of nuclear materials, such as uraninite (e.g., [9,10]).

Geochronological investigations of nuclear materials, such as those employing the ^{230}Th dating technique (e.g., [11,12]) also provide insightful forensic signatures. Investigating the geochronological history of uraninite is important to understand how uranium deposits form and develop over time. Several previous studies have adopted U-Pb age dating techniques applied to uraninite in order to unravel the complex formational history of uranium deposits (e.g., [13,14]). Application of the U-Pb geochronometer for uraninite dating does pose some important challenges that are associated with the potential loss or gain of Pb or U. Moreover, the U-Pb dating method relies on the use of a ^{238}U/^{235}U ratio that is naturally variable, and therefore propagates an additional uncertainty into the age calculation [15].

Alternatively, the secondary ^{207}Pb-^{206}Pb isochron age dating method is independent of the ^{238}U/^{235}U variance in nature, and therefore has one less source uncertainty. Pb has four isotopes 204, 206, 207, and 208; ^{204}Pb is the sole isotope that is non-radiogenic in origin, i.e., occurs in primordial abundance. ^{206}Pb and ^{207}Pb are the stable daughter products from the radioactive decay of ^{238}U and ^{235}U, respectively, whereas ^{208}Pb is produced from ^{232}Th decay. The rapid determination of accurate secondary isochron Pb-Pb ages for nuclear materials, such as uraninite, is an effective nuclear forensic tool for deciphering a sample's provenance (e.g., [16]). Traditionally, secondary Pb-Pb isochron dating of geological materials and minerals involves a labor-intensive procedure that includes sample digestion, which is then followed by separation of Pb using ion exchange chromatography; the whole process can take several weeks to complete (e.g., [17]). Alternatively, the application of laser ablation inductively coupled plasma mass spectrometry (LA-ICP-MS) technique has several advantages over the traditional, bulk digestion solution mode (SM) ICP-MS method; these include ease of sample preparation, fast throughput, and detailed chemical and isotopic information obtained at high spatial resolution (10s to 100s of micron scale, e.g., [7]). LA-ICP-MS investigations that report combined trace element and isotope data of minerals at high spatial resolution provide critical insights into open-system processes involving multiple endmember components, such as crustal contamination of granitic magmas (e.g., [18]).

On the basis of previous investigations of uranium ore deposits (e.g., [19,20]), it is clear that continental crust plays a pivotal role in the formation of U ore deposits, from providing the source of the U to the mode of occurrence (e.g., roll front vs. intrusive related). Thus, the age and type of continental material available for sourcing are important factors in controlling the isotopic (Pb, Sr, Nd) nature of the uraninite that is produced. For example, the Rb-Sr and Sm-Nd geochronometers are commonly used for age dating and provenance identification of geologic materials (e.g., [21]). Strontium has four stable isotopes (84, 86, 87, and 88) with ^{87}Sr being produced from the radioactive decay of ^{87}Rb. Accurate Rb-Sr age determinations are only obtained in a closed system. Age-corrected initial ^{87}Sr/^{86}Sr ratios (and corresponding ε_{Sr} values) provide information in relation to source region(s), even during open system behavior. For example, Varga et al. [22] investigated the Sr isotope systematics of uranium deposits worldwide; these record a large range of values that are a function of their age and variable Rb/Sr ratios.

Uranium ore deposits are impacted by a range of geochemical processes that include hydrothermal activity, metamorphism, and magmatism, and these certainly affect the various radiogenic isotope systems. Natural variations in the ^{238}U/^{235}U ratio are attributed to several factors, such as nuclear field shift, temperature, oxidation state, and source rock composition. Nuclear field

shift is a mass-independent effect used to predict the dependence of isotopic fractionation on temperature and is particularly important for heavy elements [23,24]. It has been argued previously that the difference in $^{238}U/^{235}U$ ratios between low- and high-temperature U ore deposits is related to the temperature dependence of the nuclear field shift [25,26]. As temperature increases, the magnitude of the isotope shift decreases [26]. Oxidation states also affect uranium mobility. In contrast to other oxidation dependent isotopes (e.g., Mo), the heavier ^{238}U isotope is favored in the lower oxidation state [24], thus, the U^{4+} state is linked to higher $^{238}U/^{235}U$ values. At low temperature, oxidizing fluids mobilize U^{6+} until it encounters a reducing environment resulting in the crystallization or re-crystallization of uraninite as the insoluble U^{4+} state. Uranium leached from ore during alteration/recrystallization results in minerals enriched in ^{234}U [9], and therefore the $^{238}U/^{234}U$ ratio is primarily used to evaluate recent fluid alteration events. Given the short half-life of ^{234}U, the $^{238}U/^{234}U$ ratio yields a result consistent with secular equilibrium if the deposit or mineral has not experienced alteration within the past 2.5 million years [9].

This study reports trace element abundances and Pb, Sr, and U isotopic ratios of uraninites (n = 15) from ore deposits within North America and one from the Democratic Republic of the Congo in relation to establishing baseline signatures for nuclear forensic applications. Secondary Pb-Pb isochron ages for several uraninite samples were obtained by both SM- and LA-multicollector (MC) ICP-MS. The reported ages and isotopic ratios are discussed in relation to providing insights into possible source rock compositions and environmental conditions present during the crystallization of uraninite.

2. Materials and Methods

2.1. Sample Descriptions

Uraninite samples, examined here, are from the "Ewing Collection" housed at the University of Notre Dame. Fourteen uraninite samples are from locations throughout North America and one from Shinkolobwe, Democratic Republic of the Congo (Table 1). Several samples listed in Table 1 have been examined previously for their trace elements (i.e., REEs) and Sr isotope compositions [27,28] with the exception of those from Mitchell, Marshall 2, and Moonlight. None of the samples listed in Table 1 have previously been analyzed for their U or Pb isotope compositions.

Table 1. A list of uraninite samples, reported here, with their accompanying deposit type and source location. Uraninite sample number corresponds to the Ewing Collection sample number.

Name	Location	Sample	Type
Mitchell	Mitchell County, NC	334	Intrusive anatectic
Yancey 1	Webb Mine, Yancey County, NC	336	Intrusive anatectic
Yancey 2	Yancey County, NC	513	Intrusive anatectic
Ruggles	Ruggles Mine, Grafton, NH	344	Intrusive anatectic
Billiken	Billiken Lode, Critchell, Jefferson County, CO	522	Metamorphite monometallic vein
Jefferson	Jefferson County, CO	637	Metamorphite monometallic vein
Great Bear	Great Bear Lake, NWT, Canada	626	Metamorphite polymetallic vein
Shinkolobwe	Shinkolobwe, Congo	437	Metamorphite polymetallic vein
Marshall 1	Marshall Pass area, Gunnison County, CO	530	Metamorphite hydrothermal vein
Marshall 2	Marshall Pass area, Gunnison County, CO	531	Metamorphite hydrothermal vein
Marshall 3	Marshall Pass, CO	623	Metamorphite hydrothermal vein
Marshall 4	Near Sargents, CO	624	Metamorphite hydrothermal vein
Orphan	Orphan Lode, Grand Canyon, AZ	1304	Collapsed Breccia
Skyline	Skyline Mine, Monument Valley, UT	625	Sandstone Tabular
Moonlight	Moonlight Mine, AZ	815	Sandstone Basal

The uraninite from the counties of Yancey and Mitchell (NC, USA) are both hosted by the Spruce Pine pegmatite, which crosscuts Precambrian age interlayered mica and amphibole gneiss and schist [29]. The uraninite from Ruggles Mine in Grafton County (NH, USA) occurs as dendritic intergrowths

within a pegmatite hosted by Devonian-aged Littleton Formation; the latter consists of quartz-mica schist, quartzite, amphibolite, and other high-grade metamorphic rock [30–32].

The Great Bear uraninite is hosted by late Aphebian-aged units comprised of pumice-dominated pyroclastic flows with subordinate ash and plutons within the Great Bear Lake region of Northwest Territories (Canada). This region is known for the occurrence of several U-Ag-Bi-Cu-Co-Ni-As minerals that are found within quartz and carbonate gangue [33]. Several remobilization events have been recorded at the Echo Bay location that are associated with a diabase intrusion [34,35]. The Shinkolobwe Mine (Democratic Republic of the Congo) is part of the Shaban area of the Katanga system, known for ore deposits of U, Cu, Co, and Ni. Fractures that occur within dominantly siliceous dolomite, and dolomitic and carbonaceous shales partially affected by Mg-metasomatism are host to the uraninite mineralization [34,35].

Four uraninite samples (Marshall 1, 2, 3, and 4) are investigated from the areas of Marshall Pass and Sargents, Colorado (USA). Hydrothermal activity resulted in the formation of colloform and fine-grained uraninite within fault-controlled veins and breccia zones of Pennsylvanian-aged limestone proximal to intersections of Proterozoic and Paleozoic sequences [36,37]. Billiken Lode and Jefferson uraninite are both from Jefferson County (CO, USA) from deposits that contain complexly folded and faulted Proterozoic metasediments, which host uraninite and accessory minerals ankerite, quartz, calcite, and potassium feldspar [35,36].

The uraninite within the collapse breccia structure from Orphan Lode (Grand Canyon National Park, AZ, USA) is found disseminated within the Pennsylvanian and Permian host rock matrix of limestone, sandstone, and shale [38,39]. Moonlight Mine ore (Navajo County, AZ, USA) occurs as both grains and cement and is found within an Upper Triassic channel deposit of sandstone and conglomerate. Skyline Mine uraninite (Monument Valley, UT, USA) is located within tabular sandstones of Upper Triassic age of the Chinle Formation [40].

2.1.1. Uranium Deposits

Uraninite occurrences on a global scale are categorized by their respective deposit type and subtype using the classification scheme outlined by the International Atomic Energy Agency (IAEA) [2]. Deposit types that were classed using an older identification system have been renamed, for example, "vein type" is no longer a utilized term. A total of thirteen types are investigated, here, and are listed below with respect to their temperature of formation (from high to low): intrusive, granite-related endogranitic, granite-related perigranitic, polymetallic iron oxide breccia complex, volcanic-related, metasomatite, metamorphite-monometallic, metamorphite-polymetallic, Proterozoic unconformity basement-hosted, Proterozoic unconformity contact, palaeo-quartz-pebble conglomerate, collapse breccia pipe, and sandstone (Table 1). Several U ore deposit types are not listed in Table 1, however, these are described below since they are cited in the discussion section for comparative purposes.

Intrusive deposits usually form as a result of either partial melting or fractional crystallization [41]. Intrusive deposits included in this study are from pegmatites and are considered high-grade ore [2]. Granite-related endogranitic deposits are located within veins or disseminations within the granite. Granite-related perigranitic deposits originate in veins surrounding the granitic plutons [2]. Low grade ore is produced in polymetallic iron oxide breccia complex deposits; these are broadly linked to iron oxide-copper-gold deposits. Volcanic-related deposits occur within or near volcanic calderas filled with volcanic sediments and consist of medium grade ores. Metasomatite deposits, which are associated with low to medium grade ore, are related to Na- or K-metasomatism.

Metamorphite deposits involve fluids characterized by higher temperatures, 200 to 400 °C [24], and these are variable in grade, size, and tonnage. Metamorphite deposits that are structure-bound (examined here) occur as monometallic veins associated with traces of other metallic minerals, or as polymetallic veins found with Co, Cu, Fe, Mo, Ni, Pb, Zn, Ag, and As metallics [2]. Uraninite from metamorphite deposits, examined here, that formed within hydrothermal environments are associated with lower temperatures of formation than typical metamorphites. Uranium deposits that occur immediately above, below, or span an unconformable contact that separates Archean-

Paleoproterozoic crystalline basement rock from Proterozoic red beds are defined as Proterozoic unconformity deposits. Unconformity contact deposits are situated directly above the unconformity at the base of the overlying sediment, whereas basement-hosted deposits are found below the unconformity in metasedimentary rocks [2].

Palaeo quartz-pebble conglomerate deposits consist of uraninite and brannerite hosted in pyrite-rich quartz-pebble conglomerates [2]. Collapse breccia pipe deposits produce high-grade ore within cylindrical, vertical filled pipes in sedimentary basins; currently the only known examples are within the Grand Canyon region of the USA sandstone deposits, which form at ambient temperatures when ground water removes and transports the mobile U^{6+} through the sandstone until a reductant is encountered; consequently, U^{4+} minerals form, such as uraninite [24]. Several episodes of mobilization and crystallization can occur in a single sandstone deposit resulting in several generations of uraninite.

2.2. Methods

2.2.1. In Situ Pb Isotope Ratios by LA-MC-ICP-MS

Small portions (~1 cm^2) of uraninite were cut and placed fresh surface down into a 1 inch round mount that was then filled with epoxy and cured before being polished. X-ray fluorescence (XRF) elemental maps were generated using an EDAX Orbis Micro EDXRF with the following conditions: 40 kV voltage, 300 μA, and 100 μs dwell time. XRF maps were used to identify viable areas with sufficient Pb abundances for laser ablation (LA) MC-ICP-MS measurements. In situ Pb isotopes were obtained using a Nu Plasma II MC-ICP-MS instrument located within Midwest Isotope and Trace Element Research Analytical Center (MITERAC) at the University of Notre Dame. Analyses were conducted using 25 μm spot sizes at 8 Hz and corresponding energy density of ~10 to 11 J/cm^2. Groupings of 5 ablations of samples were bracketed by the amazonite feldspar in-house standard to monitor and correct for instrumental drift and mass bias (procedure after [42,43]).

2.2.2. Bulk Sample Trace Element Abundances by ICP-MS

For each sample of uraninite, aliquots were separated by hand picking, then powdered and digested for SM-ICP-MS and SM-MC-ICP-MS analyses. When possible, the samples were separated into ”pristine’ and ”altered” fractions based on color, morphology, and luster. For example, lustrous black portions were considered pristine sections of samples, whereas yellow and orange fractions were deemed altered uraninite or containing secondary-U minerals. Approximately 50 mg of powdered sample was placed into 15 mL, precleaned Savillex© Teflon beakers for digestion using ~4 mL of high purity, concentrated HNO_3 produced with the use of a Savillex© DST-1000, sub-boiling, acid purification system. Aliquots from the digested solutions were used for both trace element concentrations and isotopic measurements. Solution mode analyses were conducted on a Nu Instruments Attom high resolution (HR) ICP-MS operating at medium mass resolution ($M/\Delta M \approx 2500$). A standard-spike addition method was employed to correct for matrix effects and instrumental drift (after [44]). Trace element abundance determinations using the analytical method, adopted here, were validated by Balboni et al. [28] based on repeated analyses of CUP2 (uranium oxide concentrate) certified reference material, both with and without chemical separation of the U-rich matrix via ion exchange chromatography.

2.2.3. Bulk Sample Pb, Sr, and U Isotope Ratios by SM-MC-ICP-MS

Pb was isolated by processing digested samples through ion exchange chromatography using AG1-X8 (200 to 400 mesh) resin following the procedure by Manhès et al. [45]. The analytical protocol for determining the Pb isotope compositions followed that of Simonetti et al. [46]. The purified Pb aliquot was spiked with a NIST SRM 997 thallium standard solution (2.5 ppb) prior to aspiration into the MC-ICP-MS instrument. Pb and Tl isotopes and ^{202}Hg were measured using seven Faraday cups on the Nu Plasma II MC-ICP-MS instrument. The $^{205}Tl/^{203}Tl$ was measured for monitoring the instrumental mass bias (exponential law, $^{205}Tl/^{203}Tl = 2.3887$), and ^{202}Hg was recorded for the ^{204}Hg

interference correction on ^{204}Pb. Prior to sample introduction, a baseline measurement of the gas and acid blank ("on-peak-zero") was conducted for 30 s. Data acquisition involved 2 blocks of 25 scans (each scan was 10 s). A 25 ppb solution of the NIST SRM 981 Pb standard (spiked with 6 ppb NIST SRM 997 Tl standard) was also analyzed periodically throughout the analytical session. Repeated measurements (n = 4) of the NIST SRM 981 + Tl standard solution yielded the following average values and associated (2σ) standard deviations: ^{206}Pb/^{204}Pb = 16.935 ± 0.003, ^{207}Pb/^{204}Pb = 15.488 ± 0.002, and ^{208}Pb/^{204}Pb = 36.686 ± 0.008.

For Sr separation, the ion exchange columns contained 1.7 mL of 200 to 400 mesh AG50W-X8 resin following a modified procedure by Crock et al. [47]. The resin bed volume was cleaned with high purity 6N HCl and 18 MΩ cm^{-2} H_2O and, then, conditioned with 5 mL of high purity 2.5N HCl. The sample aliquot was, then, loaded onto the resin in 0.25 mL of 2.5N HCl, washed with 9.75 mL of 2.5N HCl, and eluted with 4 mL of 2.5N HCl. Subsequent to ion exchange separation, the Sr-bearing aliquots were dried down and later taken up in 2% HNO_3 (~2 mL) and aspirated into the ICP torch using a desolvating nebulizing system (DSN-100, Nu Instruments Inc., Wrexham, United Kingdom). Strontium isotope measurements were conducted using a Nu Plasma II MC-ICP-MS instrument following the protocol outlined in Balboni et al. [27]. Strontium isotope data were acquired in static, multicollection mode using 5 Faraday collectors for a total of 400 s, consisting of 40 scans of 10 s integrations. Accuracy and reproducibility of the analytical protocol were verified by the repeated analysis of a 100 ppb solution of the NIST SRM 987 strontium isotope standard during the course of this study, which yielded an average value of 0.71025 ± 0.00004 (n = 4). The ε_{Sr} values, reported here, are calculated using ^{87}Sr/^{86}Sr initial ratios for the samples and the following equation:

$$\varepsilon_{Sr} = \left(\frac{Sr_{initial}}{BABI} - 1\right) \times 1000, \quad (1)$$

where BABI (basaltic achondrite best initial) ^{87}Sr/^{86}Sr = 0.69908 [48].

Uranium was purified from digested uraninite samples using UTEVA resin as outlined in Martinelli et al. [49]. Two Faraday collectors were used to measure the ^{238}U and ^{235}U ion signals, whereas the ^{234}U ion signal was recorded on a discrete dynode secondary electron multiplier. Ion signals were collected for 40 scans of 10 s integrations each (400 s total). Analyses were conducted using a standard-sample bracketing technique. Instrumental mass bias corrections employed the exponential law and the certified ^{238}U/^{235}U, ^{238}U/^{234}U, and ^{235}U/^{234}U ratios for the CRM 112A standard (New Brunswick Laboratory, Argonne, IL, USA). The internal in-run precision (2σ level) was orders of magnitude lower than the calculated external reproducibility based on the repeated measurements of the CRM 112A standard, and thus the latter uncertainties were reported, here. Delta values for the U isotope measurements were determined using the following equation:

$$\delta^x U = \left(\frac{sample}{standard} - 1\right) \times 1000, \quad (2)$$

where x represents the isotope ratio of interest (^{238}U/^{235}U or ^{234}U/^{238}U). The δ^{238}U values, calculated here, use the CRM 112A standard certified ^{238}U/^{235}U value of 137.849 (Brunswick Laboratory). The δ^{234}U value is calculated using the CRM 112A standard secular equilibrium ^{234}U/^{238}U value of 5.4970 × 10^{-5} [50]. Additionally, method validation was established by Spano et al. [51] by repeated measurement of uranium standards IRMM-184 (natural U) and IRMM-185 (enriched ^{235}U ~1.97%) using the analytical protocol, adopted here, and these yielded an external reproducibility (2σ level) of between 0.73‰ and 0.99‰, 13.6‰ and 3.4‰, and 9.3‰ and 5.6‰ for the ^{238}U/^{235}U, ^{234}U/^{238}U, and ^{235}U/^{234}U ratios, respectively.

3. Results

3.1. Trace Element Abundances

Table 2 lists the trace element abundances determined for the uraninite samples, investigated here. Figure 1 illustrates various trace element ratios and initial ^{87}Sr/^{86}Sr of the uraninite samples, investigated here, as a function of their deposit type. These ratios indicate the relative preferential incorporation of trace elements into uraninite, and are compared to canonical values for lower,

middle, and upper crust [52], and crustal sediments [53,54]. Figure 1a indicates that uraninite samples from metamorphite deposits are characterized by the highest initial $^{87}Sr/^{86}Sr$ values followed by (in order of decreasing ratios) those from metamorphite-hydrothermal, intrusive, collapsed breccia, and sandstone. Compared to the La/Yb values for continental crust [52], those for most of the uraninite samples, investigated here, are lower (Figure 1a). For the same uraninite sample, analyses of altered fractions yield higher La/Yb values as compared with their pristine counterparts (open vs. filled symbols in Figure 1a and Table 2). Figure 1b indicates that Zr abundances are higher relative to both Nb and Hf contents for the uraninite samples, investigated here; relative to continental crust, uraninite samples, studied here, have comparable Zr/Nb ratios but higher Zr/Hf values (Figure 1b). Uraninite samples that are associated with abundant zircons (Ruggles and Mitchell intrusive pegmatite deposits) exhibit higher Hf contents (Table 2) and, consequently, lower Zr/Hf values. Figure 1c demonstrates that Zr/Hf ratios are at least an order of magnitude higher than their corresponding Rb/Cs values. Ruggles and Mitchell uraninite samples contain similar Zr/Hf ratios relative to continental crust and sediments (Table 2). The data in Figure 1d (and Table 2) indicates that altered fractions of the uraninite samples contain higher Nb and Ta abundances relative to their corresponding pristine aliquots.

Table 2. Trace element abundances (ppm) determined by solution mode (SM) inductively coupled plasma mass spectrometry (ICP-MS).

Sample Name	Rb	Sr	Y	Zr	Nb	Cs	Ba	La	Yb	Hf	Ta	La/Yb	Zr/Nb	Zr/Hf	Rb/Cs	Y/Nb	Yb/Ta
Intrusive																	
334A	29.1	749	910	2694	17.0	5.6	133	64.3	31.7	97.6	1.1	2.03	159	28	5.2	54	29
336	11.8	307	42576	1119	4.4	0.5	103	242	166	1.6	bdl	1.46	252	684	23.5	9597	bdl
513A	16.1	188	21079	509	8.0	14.0	286	158	590.2	0.3	0.0	0.27	63	1737	1.1	2621	bdl
344	29.6	577	1043	109627	6.8	2.4	60.0	5.0	117	3114	1.0	0.04	16163	35	12.4	154	121
344A	157	375	197	15659	10.9	16.4	104	2.0	32.7	680	3.1	0.06	1435	23	9.6	18	11
Metamorphite																	
522	20.6	1089	5949	70968	23960	8.8	31955	482	235	67.9	32.5	2.05	3	1045	2.3	0.2	7
522A	156	316	21.1	363	71.8	0.6	4147	68.0	10.8	5.1	2.2	6.28	5	71	249.1	0.3	5
637	35.5	304	860	6356	427	3.6	566	84.6	65.7	38.5	6.7	1.29	15	165	9.9	2	10
637A	37.2	403	422	7230	730	3.1	289	59.7	22.1	39.5	32.8	2.69	10	183	12.0	1	1
626	21.4	146	27454	5530	42.4	4.3	1792	1315	548	5.7	bdl	2.40	130	964	5.0	648	bdl
626A	26.4	109	3871	6162	86.8	0.7	2431	287	74.2	5.9	0.1	3.86	71	1049	40.3	45	742
437B	12.2	967	5575	1587	37.7	5.1	19.8	210	39.8	1.7	bdl	5.28	42	959	2.4	148	bdl
Hydrothermal																	
530	29.0	217	727	5825	1997	3.7	248	87.9	89.9	43.0	1.9	0.98	2.9	136	7.8	0.4	48
530A	93.7	108	31.3	877	909	5.5	422	23.0	6.2	9.4	0.7	3.73	1.0	93.2	17.2	0.0	9
531	33.2	450	1428	9819	5871	19.6	181	256	145	42.8	2.4	1.76	1.7	229	1.7	0.2	61
531A	40.5	660	635	6490	5144	20.1	620	183.9	78.0	37.5	1.6	2.36	1.3	173.1	2.0	0.1	49
623	32.9	306	1308	8319	3106	14.1	153	147	131	49.4	1.9	1.12	2.7	168	2.3	0.4	69
623A	54.0	200	147	3584	2282	22.1	263	44.2	18.0	35.4	1.7	2.46	1.6	101.1	2.4	0.1	11
624	36.5	320	1069	4023	3762	15.2	174	127	142	32.0	10.7	0.90	1.1	126	2.4	0.3	13
624A	59.4	313	77.9	3635	4656	17.3	2578	69.1	17.4	35.2	5.9	3.97	0.8	103.3	3.4	0.0	3
Collapsed Breccia																	
1304B	40.7	60	2798	177	7.9	11.6	5173	30.7	19	3.0	bdl	1.60	22	58	3.5	353	bdl
Sandstone																	
625	33.6	273	3720	3064	54.4	4.9	26.8	522	259	4.8	0.1	2.02	56	644	6.9	68	2587
625A	32.6	313	108	450	64.4	2.1	20.7	239.8	4.3	0.4	0.4	55.36	7	1264	15.4	2	11
815B	61.7	997	722	57	12.5	3.0	3731	644	7.2	0.5	0.2	88.9	5	125	20.7	58	36
Upper Cont. Crust	82	320	21	193	12	4.9	628	31	2	5.3	0.9	15.50	16	36	16.7	2	2
Mid. Cont. Crust	65	282	20	149	10	2.2	532	24	2.2	4.4	0.6	10.91	15	34	29.5	2	4
Lower Cont. Crust	11	348	16	68	5	0.3	259	8	1.5	1.9	0.6	5.33	14	36	36.7	3	3

Table 2. *Cont.*

Sample Name	Rb	Sr	Y	Zr	Nb	Cs	Ba	La	Yb	Hf	Ta	La/Yb	Zr/Nb	Zr/Hf	Rb/Cs	Y/Nb	Yb/Ta
Bulk Cont. Crust	49	320	19	132	8	2	456	20	1.9	3.7	0.7	10.53	17	36	24.5	2	3
River	113	-	-	191	17.1	8.84	635	43.3	-	5.77	1.39	-	11.2	33.1	12.8	-	-
Loess	73	-	-	302	12.7	3.8	458	27.9	-	8.9	0.92	-	23.8	33.9	19.2	-	-
NASC	125	142	-	200	-	5.2	636	31.1	3.06	6.3	1.12	10.16	-	31.7	24.0	-	2.7
PAAS	160	-	-	210	18	6	650	38.2	-	5	1.28	-	11.7	42.0	26.7	-	-
Russian	144	-	-	213	14	-	677	33.5	-	6.6	-	-	15.2	32.3	-	-	-
CondieF	163	-	-	201	15.4	-	551	38.8	-	4.6	1.4	-	13.1	43.7	-	-	-
GLOSSg	57.2	-	-	130	8.94	3.48	776	28.8	-	4.06	0.63	-	14.5	32.0	16.4	-	-
PM	235	-	-	168	14.2	4.78	823	33	-	5.45	-	-	11.8	30.8	49.2	-	-
AM	141	-	-	155	9.7	5.57	646	26.1	-	4.96	-	-	16.0	31.3	25.3	-	-
Tillite	80	-	-	167	9.4	2.6	476	25.7	-	4.37	0.61	-	17.8	38.2	30.8	-	-
Condie	25	-	-	105	4	-	150	10.3	-	3.1	0.3	-	26.3	33.9	-	-	-
Condie	90	-	-	147	10	-	625	28	-	3.8	0.83	-	14.7	38.7	-	-	-
PM	61	-	-	285	7.71	1.42	403	27.2	-	9.68	-	-	37.0	29.4	43.0	-	-
AM	67	-	-	155	6.73	2.57	441	20.7	-	4.73	-	-	23.0	32.8	26.1	-	-

[1] bdl, below detection limit; (-), value not reported; A, altered; B, bulk; crustal values are from Rudnick and Gao [52]; sediment values are from McLennan [53] and Gromet et al. [54].

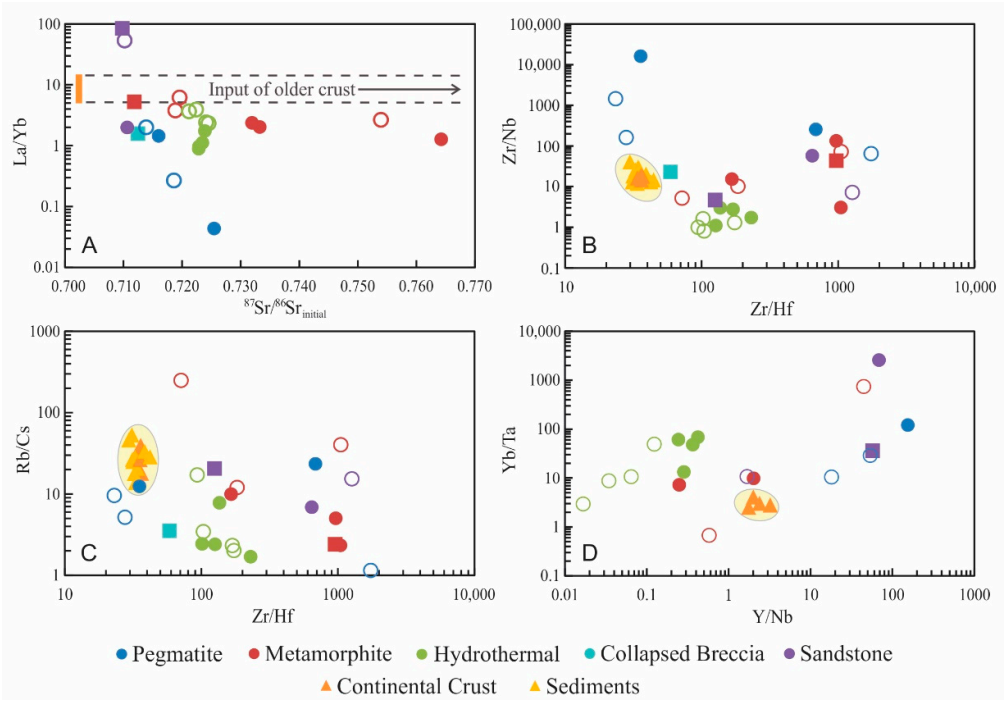

Figure 1. Binary plots illustrating trace element concentration ratios (determined using solution mode ICP-MS) for uraninite based on deposit type. (**A**) $^{87}Sr/^{86}Sr_{initial}$ vs. La/Yb, orange rectangle indicates range of La/Yb values for continental crust; (**B**) Zr/Hf vs. Zr/Nb; (**C**) Zr/Hf vs. Rb/Cs; (**D**) Y/Nb vs. Yb/Ta. Solid circles represent pristine fraction of uraninite, whereas open circles denote altered areas, and square symbols indicate bulk aliquots as pristine and altered segments could not be physically separated. The yellow fields (orange triangles) denote values for crust [52] and sediment [53,54].

3.2. Secondary Pb-Pb Isochron Ages

Pb isotope ratios obtained by SM- and LA-MC-ICP-MS are listed in Tables 3 and 4, respectively. Selected secondary Pb-Pb isochrons based on both SM- and LA-MC-ICP-MS-generated data were produced using Isoplot (v. 4.0; [55]) and are shown in Figure 2 (see Figure S1 for all other Pb-Pb isochrons for remaining samples).

Table 3. Isotopic Pb ratios determined by solution mode (SM) multicollector (MC) ICP-MS.

Sample	$^{206}Pb/^{204}Pb$	2σ	$^{207}Pb/^{204}Pb$	2σ	$^{208}Pb/^{204}Pb$	2σ	$^{207}Pb/^{206}Pb$	2σ	$^{208}Pb/^{206}Pb$	2σ
Intrusive										
334	19,536	2060	1069.3	111.4	240	22.4	0.0546	0.000011	0.0121	0.000023
334A	697	0.0502	52.26	0.010	46.24	0.010	0.0750	0.000002	0.0664	0.000002
336	20,989	1136	1148.7	61.8	221	11.1	0.0547	0.000027	0.0105	0.000072
513A	13,509	70	740	3.82	65.96	0.316	0.0548	0.000003	0.0049	0.000005
344	7051	16.5	388.4	0.904	52.43	0.119	0.0551	0.000002	0.0074	0.000003
344A	9760	10.3	532	0.56	57.01	0.053	0.0545	0.000001	0.0058	0.000002
Metamorphite										
522	36.5	0.011	16.97	0.005	38.90	0.011	0.4649	0.000037	1.0657	0.000050
522A	32.2	0.0010	16.72	0.0007	38.82	0.002	0.5190	0.000010	1.2053	0.000032
637	53.3	0.004	17.78	0.002	38.97	0.004	0.3339	0.000008	0.7317	0.000027
637A	46.7	0.0059	17.49	0.001	38.99	0.003	0.3747	0.000033	0.8353	0.000087
626	40,711	306	3803	28.6	36.02	0.254	0.0934	0.000002	0.0009	0.000001
626A	24,862	132.8	2313	12.34	35.94	0.141	0.0930	0.000006	0.0014	0.000004
437B	235,358	41,200	14,209	2480	58.42	6.56	0.0604	0.000003	0.0003	0.000011
Hydrothermal										
530	94.9	0.004	19.78	0.0010	40.47	0.003	0.2086	0.000004	0.4266	0.000013
530A	66.5	0.001998	18.42	0.0006	40.49	0.001	0.2771	0.000003	0.6091	0.000010
531	101.3	0.018	20.10	0.0022	40.33	0.004	0.1984	0.000018	0.3981	0.000065
531A	92.6	0.003	19.68	0.0007	40.32	0.002	0.2125	0.000002	0.4353	0.000008
623	89.0	0.013	19.51	0.0024	40.46	0.005	0.2190	0.000008	0.4544	0.000022
623A	61.4	0.058	18.22	0.0061	40.45	0.015	0.2965	0.000202	0.6585	0.000640
624	151.0	0.054	22.43	0.0066	40.40	0.007	0.1485	0.000013	0.2676	0.000065
624A	104.7	0.018	20.20	0.0029	40.25	0.006	0.1929	0.000011	0.3845	0.000032
Collapsed Breccia										
1304B	426.1	0.662	38.04	0.055	39.11	0.059	0.0893	0.000030	0.0917	0.000073
Sandstone										
625	110.2	0.014	20.35	0.003	38.55	0.005	0.1846	0.000007	0.3496	0.000018
625A	98.2	0.005	19.77	0.0011	38.52	0.003	0.2013	0.000005	0.3924	0.000013
815B	843	0.61	58.73	0.039	38.51	0.023	0.0696	0.000006	0.0456	0.000014

[1] A = altered; B = bulk.

Table 4. Isotopic Pb ratios obtained by laser ablation (LA) MC-ICP-MS and wt% UO_2 and PbO determined by electron microprobe (EMP).

Sample_Location	$^{206}Pb/^{204}Pb$	2σ	$^{207}Pb/^{204}Pb$	2σ	$^{208}Pb/^{204}Pb$	2σ	$^{207}Pb/^{206}Pb$	2σ	$^{208}Pb/^{206}Pb$	2σ	wt% UO_2	wt% PbO
Intrusive												
334_17	94,938	13,465	5145	729	1019	142	0.0542	0.000014	0.01076	0.00003	71.1	3.64
334_21	123,511	53,664	6688	2904	2010	854	0.0542	0.000004	0.01638	0.00019	78.3	4.04
334_26	118,349	29,486	6395	1594	1173	292	0.0540	0.000003	0.00991	0.000002	83.1	3.84
334_3	147,991	7843	8003	423	1083	57	0.0541	0.000003	0.00732	0.000002	66.7	5.42
334_22	474	0.86	40.15	0.05	43.57	0.02	0.0847	0.000056	0.09186	0.00013	36.5	0.86
336_1a	36,406	69,797	1968	3762	484	918	0.0540	0.000005	0.01315	0.00002	-	-
336_2	41,744	76,285	2251	4132	549	992	0.0540	0.000005	0.01297	0.00002	-	-
336_3	122,925	81,790	6635	4425	1654	1094	0.0540	0.000004	0.01332	0.00001	-	-
336_4	78,763	152,570	4252	8245	1019	1991	0.0540	0.000005	0.01306	0.00001	-	-
336_5	84,114	70,387	4535	3801	962	802	0.0539	0.000005	0.01140	0.00002	-	-
336_6	188,717	112,461	10,189	6082	2171	1233	0.0540	0.000007	0.01041	0.00001	-	-
344_57	32,570	1274	1738	67.2	126	3.71	0.0534	0.000023	0.00391	0.00004	90.2	4.11
344_7	44,742	1735	2382	92.2	134	4.25	0.0532	0.000009	0.00305	0.00003	88.1	4.09
344_12	136,303	75,079	7216	3976	293	161	0.0529	0.000004	0.00213	0.000005	85.9	4.69
344_28	17,532	202	942	10.80	72.1	0.68	0.0537	0.000011	0.00412	0.00002	89.8	3.53
344_21	17,202	311	923	16.33	73	0.81	0.0537	0.000022	0.00429	0.00004	88.1	4.14
Metamorphite												
522_8	38.5	0.01	17.0	0.001	38.79	0.002	0.4414	0.000130	1.00648	0.00034	67.8	1.33
522_17	38.4	0.02	17.0	0.002	38.76	0.004	0.4420	0.000236	1.00817	0.00059	60.4	2.46
522_27	39.7	0.05	17.1	0.003	38.78	0.002	0.4301	0.000521	0.97802	0.00133	48.3	1.50
522_10	37.3	0.04	16.9	0.002	38.74	0.002	0.4531	0.000471	1.03811	0.00120	74.5	6.12
637_15a	66.16	0.008	18.39	0.0024	38.94	0.0051	0.2779	0.000029	0.58859	0.00005	-	-
637_16	61.64	0.006	18.17	0.0019	38.94	0.0037	0.2948	0.000023	0.63172	0.00004	-	-
637_21b	60.63	0.006	18.12	0.0016	38.94	0.0035	0.2989	0.000021	0.64225	0.00004	-	-
637_11a	59.90	0.007	18.09	0.0017	38.94	0.0037	0.3019	0.000029	0.65006	0.00006	-	-
626_1	67,060	2824	6079	255.1	36.58	1.55	0.0907	0.00003	0.00054	0.000003	-	-
626_2	40,729	1831	3823	172.3	36.28	1.24	0.0939	0.00006	0.00090	0.00002	-	-
626_3	67,977	2330	6266	213.9	35.41	1.22	0.0922	0.00002	0.00052	0.000003	-	-
626_4	53,426	3259	4897	300.2	36.69	2.26	0.0917	0.00007	0.00069	0.000004	-	-

Table 4. *Cont.*

Sample_Location	$^{206}Pb/^{204}Pb$	2σ	$^{207}Pb/^{204}Pb$	2σ	$^{208}Pb/^{204}Pb$	2σ	$^{207}Pb/^{206}Pb$	2σ	$^{208}Pb/^{206}Pb$	2σ	wt% UO_2	wt% PbO
626_5	53,378	2528	4971	235.5	39.28	1.92	0.0932	0.00003	0.00072	0.00001	-	-
626_6	53,837	3061	4969	282.6	37.20	2.13	0.0923	0.00004	0.00069	0.000004	-	-
626_7	55,104	3617	5121	337.9	40.88	2.77	0.0929	0.00032	0.00073	0.000003	-	-
626_8	71,447	13,204	6632	1228	33.56	6.68	0.0928	0.00005	0.00048	0.000002	-	-
626_9	72,512	5969	6853	564	38.30	3.16	0.0945	0.00004	0.00053	0.000001	-	-
626_10	44,305	19,153	3991	1727	26.29	11.13	0.0901	0.00004	0.00058	0.00001	-	-
626_11	10,249	14,152	955.2	1320	11.56	7.46	0.0932	0.00006	0.00090	0.00001	-	-
626_12	529.71	7076	46.468	660	1.25	3.38	0.0931	0.00009	0.00046	0.00001	-	-
626_13	49,435	2727	4568	247	40.60	2.24	0.0930	0.00029	0.00082	0.000002	-	-
626_14	58,444	3162	5487	297	42.14	2.28	0.0939	0.00004	0.00072	0.000002	-	-
626_15	58,476	3616	5490	340	39.11	2.60	0.0938	0.00004	0.00066	0.000002	-	-
437_12	8520	66,789	508	4026	-0.37	1.54	0.0602	0.000007	0.00002	0.000001	88.5	7.10
437_17	187,980	128,045	11,340	7718	6.82	5.11	0.0603	0.000007	0.00004	0.0000004	86.5	7.21
437_28	36,307	65,603	2178	3947	1.49	1.49	0.0600	0.000009	0.00002	0.000001	88.9	7.22
437_19	76,328	71,136	4601	4281	3.96	3.98	0.0603	0.000007	0.00006	0.000001	87.9	7.35
437_20	40,121	61,256	2419	3692	0.69	0.86	0.0603	0.000006	0.00001	0.000001	88.2	6.89
Hydrothermal												
530_12	130.1	1.19	21.43	0.065	40.51	0.04	0.1649	0.001062	0.31185	0.00290	76.7	0.51
530_15	143.6	0.06	22.15	0.006	40.44	0.01	0.1542	0.000029	0.28151	0.00007	87.7	1.32
530_8	149.2	0.13	22.41	0.007	40.41	0.01	0.1502	0.000095	0.27092	0.00024	89.3	1.15
530_19	141.4	0.09	22.02	0.006	40.44	0.01	0.1558	0.000067	0.28608	0.00018	86.1	1.52
530_25	133.9	0.61	21.63	0.030	40.48	0.01	0.1616	0.000516	0.30248	0.00138	82.2	0.74
531_5	125.8	0.47	21.3	0.022	40.40	0.005	0.1695	0.000457	0.32141	0.00121	86.4	1.16
531_1	137.8	0.43	21.9	0.020	40.38	0.01	0.1589	0.000352	0.29318	0.00092	83.8	1.17
531_10	86.5	0.43	19.5	0.021	40.56	0.01	0.2250	0.000884	0.46919	0.00233	83.9	0.12
531_22	103.5	0.08	20.2	0.005	40.39	0.004	0.1953	0.000119	0.39031	0.00031	87.7	1.39
531_21	113.2	0.30	20.7	0.015	40.41	0.01	0.1826	0.000350	0.35703	0.00093	85.1	1.59
623_18	105.4	0.24	20.23	0.013	40.35	0.011	0.1919	0.000326	0.38286	0.00088	83.7	0.42
623_22	130.1	0.13	21.42	0.007	40.50	0.007	0.1646	0.000110	0.31130	0.00030	84.1	2.16

Table 4. *Cont.*

Sample_Location	$^{206}Pb/^{204}Pb$	2σ	$^{207}Pb/^{204}Pb$	2σ	$^{208}Pb/^{204}Pb$	2σ	$^{207}Pb/^{206}Pb$	2σ	$^{208}Pb/^{206}Pb$	2σ	wt% UO_2	wt% PbO
623_37	153.8	0.08	22.59	0.005	40.47	0.007	0.1468	0.000050	0.26298	0.00013	83.6	1.91
623_34	135.3	0.04	21.74	0.004	40.43	0.007	0.1606	0.000038	0.29869	0.00009	74.8	1.48
623_43	144.0	0.15	22.11	0.009	40.42	0.009	0.1536	0.000116	0.28079	0.00031	73.7	1.56
624_20	132.8	0.27	21.49	0.014	40.22	0.007	0.1618	0.000234	0.30307	0.00060	64.5	1.49
624_15	137.1	0.05	21.77	0.009	40.45	0.019	0.1587	0.000019	0.29504	0.00005	67.3	1.00
624_7	145.3	0.07	22.16	0.011	40.45	0.020	0.1525	0.000017	0.27831	0.00004	76.9	1.31
624_22	151.2	0.10	22.49	0.014	40.59	0.025	0.1488	0.000041	0.26849	0.00012	82.8	1.89
624_a	179.1	0.17	23.79	0.014	40.55	0.019	0.1329	0.000067	0.22632	0.00018	-	-
Collapsed Breccia												
1304_1	536.4	1.3	44.07	0.06	38.85	0.04	0.0822	0.0001	0.07240	0.0002	81.8	1.30
1304_6	559.0	1.5	45.82	0.08	38.83	0.05	0.0819	0.0001	0.06956	0.0002	66.3	1.18
1304_4	541.0	2.8	44.44	0.11	38.78	0.05	0.0822	0.0003	0.07179	0.0004	72.6	1.20
1304_9	724.8	5.5	52.95	0.28	38.79	0.05	0.0730	0.0002	0.05362	0.0004	78.7	1.52
1304_2	567.0	1.6	45.40	0.12	38.80	0.05	0.0800	0.0002	0.06844	0.0002	83.8	1.35
Sandstone												
625_27	109.9	0.03	20.27	0.002	38.49	0.004	0.1844	0.000034	0.35017	0.00008	62.6	1.19
625_4	115.4	0.09	20.54	0.005	38.46	0.006	0.1779	0.000103	0.33322	0.00027	73.3	1.21
625_15	122.3	0.09	20.89	0.007	38.51	0.012	0.1709	0.000086	0.31503	0.00022	93.5	0.05
625_9	122.3	0.13	20.89	0.009	38.50	0.011	0.1708	0.000124	0.31479	0.00033	86.7	0.13
625_30	111.3	0.09	20.34	0.006	38.49	0.008	0.1829	0.000104	0.34600	0.00027	80.7	0.02

[1] wt% UO_2 indicates if the analysis was taken for a pristine or altered region; (-), not analyzed; 626 analyses were previously obtained by Balboni [56].

Reported ages for the pegmatite host to the uraninites from Mitchell and Yancey counties are Paleozoic in age and range between 252 and 542 Ma [29]. A U-Pb age of 304 Ma (no associated uncertainty) is reported for uraninite from the Ruggles Mine [31]. In this study, uraninite from Mitchell and Ruggles yield Pb-Pb secondary isochron ages of 370 ± 120 Ma and 324.6 ± 8.1 Ma, respectively. In comparison, LA-MC-ICP-MS analyses of uraninite yield ages of 370 ± 110 Ma for Mitchell, 370 ± 1600 Ma for Yancey 1, and 327 ± 110 Ma for Ruggles. Given their proximal geographic location to one another in the Appalachian Mountain belt, a combined secondary Pb-Pb isochron including all three sites results in uraninite ages of 324.5 ± 1.2 Ma and 323 ± 21 Ma for SM- and LA-MC-ICP-MS methods, respectively (Figure 2).

Uraninite from the Great Bear area is the oldest documented sample investigated in this study. The Great Bear region is identified by several uranium deposits with variable ages; mineralization at Echo Bay has been dated between 1500 ± 10 and 1424 ± 29 Ma by U-Pb dating [33]. Here, we report secondary Pb-Pb isochron ages of 1509 ± 19 and 1444 ± 61 Ma for SM and LA-MC-ICP-MS-based data, respectively (Figure 2). Using SM-MC-ICP-MS, the secondary Pb-Pb isochron age of −68 ± 7.2 Ma for the uraninite from Jefferson does not agree with the reported U-Pb age of 69.3 ± 1.1 Ma for the Jefferson County Schwartzwalder deposit [57]. Similarly, the LA-MC-ICP-MS yielded a secondary Pb-Pb isochron age of 97 ± 20 Ma, which, given the associated uncertainty, overlaps with the age provided by Ludwig et al. [57]. The Billiken uraninite, also located in Jefferson County, yields a secondary Pb-Pb isochron age of 537 ± 18 Ma (SM-MC-ICP-MS) and 733 ± 1200 Ma (LA-MC-ICP-MS). Previously reported ages for uraninite mineralization within this area range between 44.0 and 444.7 Ma, with a second, younger generation of Tertiary uraninite at ~35 Ma [37]. Analyses conducted using SM-MC-ICP-MS from Marshall 1, 2, 3, and 4 yield ages of 96.84 ± 0.9 Ma, 126.8 ± 5.5 Ma, 35.9 ± 5.2 Ma, and 109.1 ± 3.3 Ma, respectively. Marshall 1, 2, 3, and 4, respectively, yield ages of 191 ± 170 Ma, 84 ± 130 Ma, 109 ± 200 Ma, and 139 ± 180 Ma by LA-MC-ICP-MS. Re-examination of the Marshall 2 LA-MC-ICP-MS analyses determined an age of lower uncertainty at 147 ± 25 Ma. Uraninite from the Skyline Mine in SE Utah records an age of 110.0 ± 8.8 Ma and 176 ± 91 Ma by SM-MC-ICP-MS and LA-MC-ICP-MS analyses, respectively. Uranium ores within SE Utah record three mineralization events, i.e., Late Triassic-Early Jurassic, Late Jurassic, and Early Cretaceous [38]. LA-MC-ICP-MS analyses of the Shinkolobwe uraninite has a secondary Pb-Pb isochron that yields an age of 617 ± 1600 Ma, which overlaps (given the large associated uncertainty) with published ages of 670 ± 20 Ma and 620 ± 10 Ma [58], while Decree et al. [34] reported an age of 652.3 ± 7.3 Ma for Sinkolobwe uraninite.

3.3. Sr Isotope Data

Sr isotope results, obtained here, are listed in Table 5. Sr concentrations for uraninite samples, investigated here, range from 60 to 1089 ppm (Table 2). All initial $^{87}Sr/^{86}Sr$ ratios are well above the present-day Bulk Earth value of 0.7045 indicative of a significant crustal signature (Table 5). The Rb-Sr isotope results yield erroneous Rb-Sr isochron ages (Figure S2). Initial $^{87}Sr/^{86}Sr$ and corresponding ε_{Sr} values, as defined above, were calculated based on the secondary Pb-Pb isochron ages, reported here. Literature values were used in the event that a secondary Pb-Pb isochron age was not determined. The ε_{Sr} values define a broad range of values between +14.4 and +114.1 (Table 5 and [59]). In Figure 3, North American craton Nd model ages based on the Bennett and DePaolo's [21] study are compared to the ε_{Sr} values calculated for uraninite investigated in this study (n = 12) and for uraninite (n = 15) analyzed previously [59]. Overall, the ε_{Sr} values increase from the margins to the central regions of the North American craton with the highest values in Canada, with the exception of uraninite from Rabbit Lake, Saskatchewan, Canada at +17.9 (Figure 3). Rabbit Lake uraninite is classified as a Proterozoic unconformity ore deposit, and thus could have experienced higher degrees of alteration during open system processes. This general trend of increasing ε_{Sr} values relative to geographic position in North America is also evident within the southwestern region of the United States (Figure 3b). In the central section of the region shown in Figure 3b, the craton age ranges between 1.8 and 2.0 Ga and corresponds to uraninite samples from 11 locations, investigated here. The ε_{Sr} values for uraninite from Skyline, Happy Jack, Big Indian, Cane Spring Canyon, and

Adair Mine are distinctively lower as compared with those from Jefferson and Marshall Pass (further to the east).

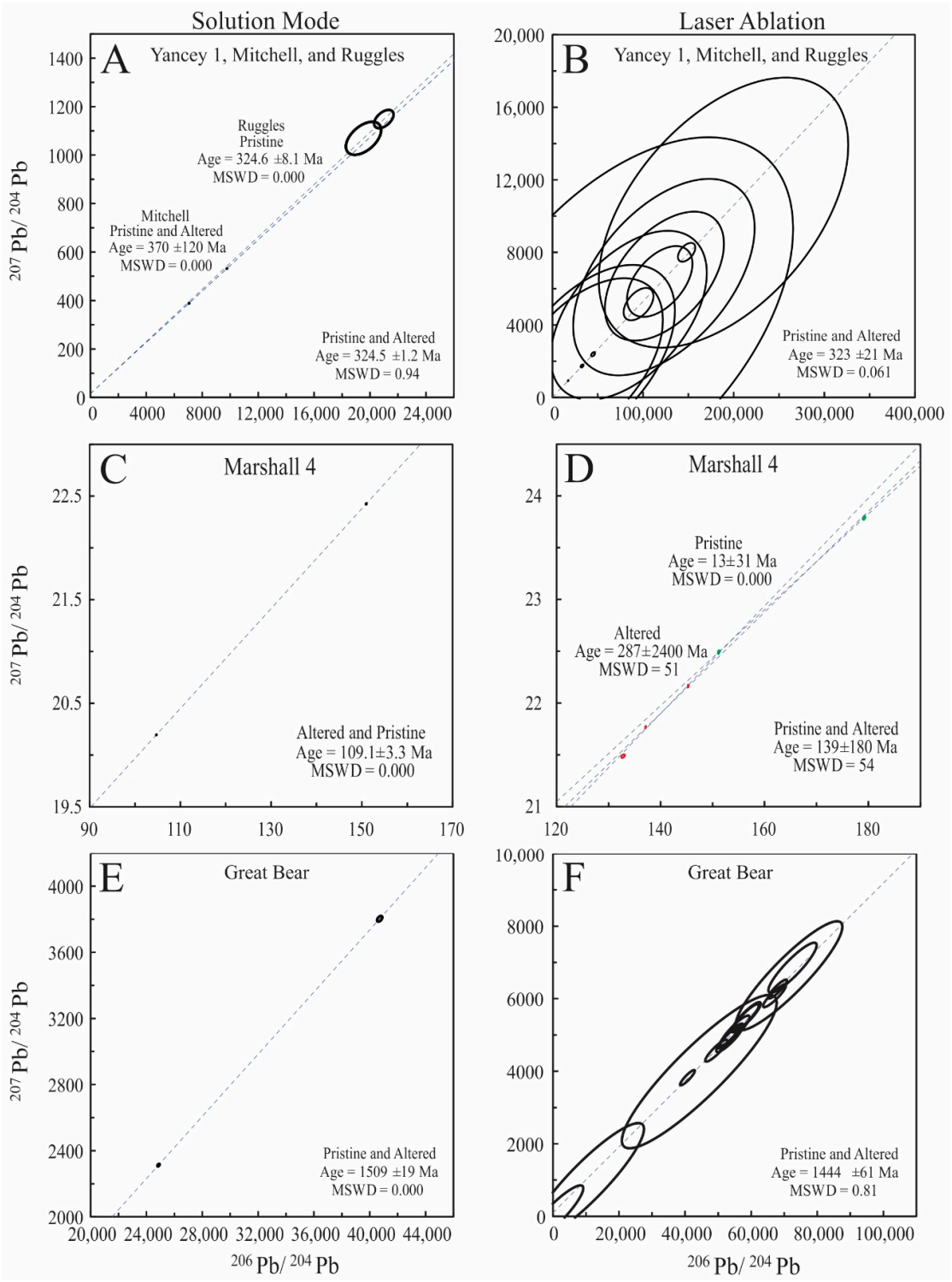

Figure 2. Secondary Pb-Pb isochrons of selected uraninite, investigated in this study. (**A**,**C**,**E**) represent analyses obtained using SM-MC-ICP-MS; whereas (**B**,**D**,**F**) illustrate results acquired by LA-MC-ICP-MS. (A,B) compare age results between pristine and altered uraninite sections from Yancey 1, Mitchell, and Ruggles, (C,D) compare ages for pristine and altered regions of uraninite from Marshall 2, and (E,F) show dating results for uraninite (pristine and altered) from Great Bear region.

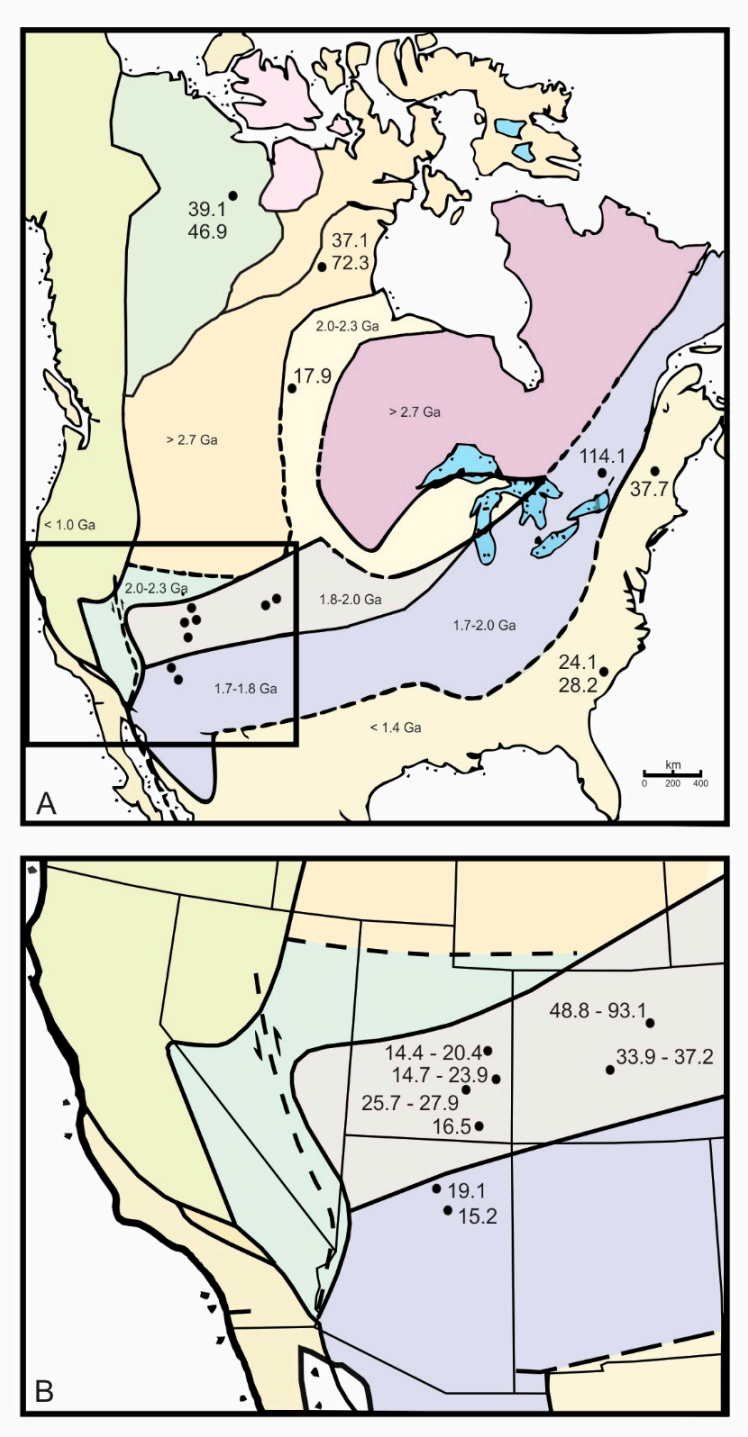

Figure 3. εSr values (as defined in text) of uraninite from this study and Corcoran et al. [59]. Colors do not have any geological significance. (**A**) Map of North American cratons with associated Nd model ages modified from Bennett and DePaolo [21]; (**B**) inset of western United States.

Table 5. Sr and U isotopic compositions obtained by SM-MC-ICP-MS.

Sample	$^{87}Sr/^{86}Sr$	2σ	$^{84}Sr/^{86}Sr$	2σ	^{85}Rb	$^{87}Rb/^{86}Sr$	$^{87}Sr/^{86}Sr_{initial}$	εSr	$^{235}U/^{238}U$	$^{238}U/^{235}U$	$^{234}U/^{238}U$	$^{234}U/^{235}U$	$^{235}U/^{234}U$	$\delta^{238}U$	$\delta^{234}U$
Intrusive															
334	-	-	-	-	-	-	-	-	0.00727	137.61	5.441×10^{-5}	0.00749	133.55	−1.76	−10.28
334A	0.71440	0.00001	0.05640	0.00002	0.00051	0.11	0.71382	21.1	0.00726	137.72	5.335×10^{-5}	0.00735	136.10	−0.95	−29.40
336	0.71653	0.00004	0.05621	0.00005	0.00007	0.11	0.71595	24.1	-	-	-	-	-	-	-
513A	0.71984	0.00003	0.05621	0.00007	0.00013	0.25	*0.71855*	*27.9*	0.00726	137.73	5.400×10^{-5}	0.00744	134.41	−0.87	−17.60
344	0.72610	0.00001	0.05624	0.00004	0.00025	0.15	0.72542	*37.7*	0.00726	137.70	5.432×10^{-5}	0.00748	133.71	−1.12	−11.75
344A	-	-	-	-	-	-	-	-	0.00725	137.84	5.481×10^{-5}	0.00756	132.25	−0.09	−2.82
Metamorphite															
522	0.73362	0.00007	0.05475	0.00008	0.00183	0.05	0.73320	48.8	0.00725	137.89	5.282×10^{-5}	0.00728	137.27	0.28	−39.05
522A	0.73036	0.00001	0.05651	0.00001	0.00035	1.44	0.71953	29.2	0.00726	137.81	5.757×10^{-5}	0.00794	125.99	−0.26	47.35
637	0.76451	0.00002	0.05634	0.00002	0.00053	0.34	*0.76418*	*93.1*	0.00725	137.85	5.450×10^{-5}	0.00751	133.12	−0.03	−8.62
637A	0.75417	0.00002	0.05628	0.00002	0.00057	0.27	0.75392	78.4	0.00726	137.74	5.332×10^{-5}	0.00734	136.16	−0.79	−30.05
626	0.74101	0.00005	0.05471	0.00005	0.00242	0.43	0.73189	46.9	0.00727	137.56	5.351×10^{-5}	0.00736	135.90	−2.08	−26.63
626A	0.73379	0.00005	0.05554	0.00006	0.00071	0.70	0.71878	28.2	0.00727	137.50	5.500×10^{-5}	0.00756	132.21	−2.52	0.63
437B	0.71208	0.00007	0.05427	0.00038	0.00183	0.04	*0.71176*	*18.1*	0.00726	137.82	5.506×10^{-5}	0.00759	131.78	−0.22	1.66
Hydrothermal															
530	0.72336	0.00002	0.05645	0.00001	0.00062	0.39	0.72283	34.0	0.00725	137.85	5.241×10^{-5}	0.00722	138.47	0.00	−46.60
530A	0.72454	0.00001	0.05634	0.00001	0.00046	2.51	0.72113	31.5	0.00726	137.72	5.483×10^{-5}	0.00756	132.35	−0.96	−2.61
531	0.72422	0.00001	0.05640	0.00002	0.00031	0.21	0.72384	35.4	0.00726	137.79	5.261×10^{-5}	0.00725	137.88	−0.43	−43.01
531A	0.72478	0.00001	0.05620	0.00004	0.00096	0.18	0.72446	36.3	0.00726	137.68	5.608×10^{-5}	0.00772	129.54	−1.24	20.11
623	0.72358	0.00001	0.05644	0.00001	0.00032	0.31	0.72342	34.8	0.00726	137.69	5.141×10^{-5}	0.00708	141.22	−1.19	−64.69
623A	0.72443	0.00001	0.05661	0.00001	0.00128	0.78	0.72404	35.7	0.00726	137.76	5.563×10^{-5}	0.00766	130.49	−0.65	12.00
624	0.72330	0.00001	0.05642	0.00001	0.00120	0.33	0.72280	33.9	0.00726	137.70	5.225×10^{-5}	0.00720	138.94	−1.11	−49.46
624A	0.72318	0.00002	0.05639	0.00001	0.00031	0.55	0.72234	33.3	0.00725	137.99	5.488×10^{-5}	0.00757	132.07	1.00	−1.72
Collapsed Breccia															
1304B	0.71555	0.00002	0.05646	0.00001	0.00055	1.97	*0.71240*	*19.1*	0.00726	137.74	5.366×10^{-5}	0.00739	135.28	−0.81	−23.78
Sandsonte															
625	0.71113	0.00002	0.05604	0.00004	0.00045	0.36	0.71059	16.5	0.00725	137.98	5.201×10^{-5}	0.00718	139.29	0.95	−53.84
625A	0.71060	0.00002	0.05655	0.00001	0.00042	0.30	0.71014	15.8	0.00734	136.19	5.532×10^{-5}	0.00754	132.71	−12.01	6.45
815B	0.71016	0.00001	0.05639	0.00002	0.00041	0.18	*0.70971*	*15.2*	0.00725	137.85	5.413×10^{-5}	0.00746	133.99	−0.03	−15.25

[1] (-), not analyzed; italicized number indicates an initial $^{87}Sr/^{86}Sr$ value derived from literature data; A, altered; B, bulk.

Uraninite samples linked to a pegmatitic origin can be separated into two groups (Figure 3a and Table 5). Uranium deposits located within the eastern coastal region of the USA, where craton ages are <1.4 Ga, are linked to ε_{Sr} values that range between +24.1 and +37.7; whereas uraninite with ε_{Sr} values of +72.3 (>2.7 Ga) and +114.1 (1.7 to 2.0 Ga) are from deposits located within the older cratons of Canada (Figure 3a).

Uraninite samples linked to a pegmatitic origin can be separated into two groups (Figure 3a and Table 5). Uranium deposits located within the eastern coastal region of the USA, where craton ages are <1.4 Ga, are linked to ε_{Sr} values that range between +24.1 and +37.7; whereas uraninite with ε_{Sr} values of +72.3 (>2.7 Ga) and +114.1 (1.7–2.0 Ga) are from deposits located within the older cratons of Canada (Figure 3a).

Bataille and Bowen [60] modeled the $^{87}Sr/^{86}Sr$ variation of bioavailable Sr (i.e., isoscape maps) across the USA, which are based on reported literature values for various types of geologic samples (rock lithologies, fluvial, and vegetation). Figure 4 superimposes the sample locations and corresponding ε_{Sr} values for samples investigated in this study within the USA isoscapes map from Bataille and Bowen [60].

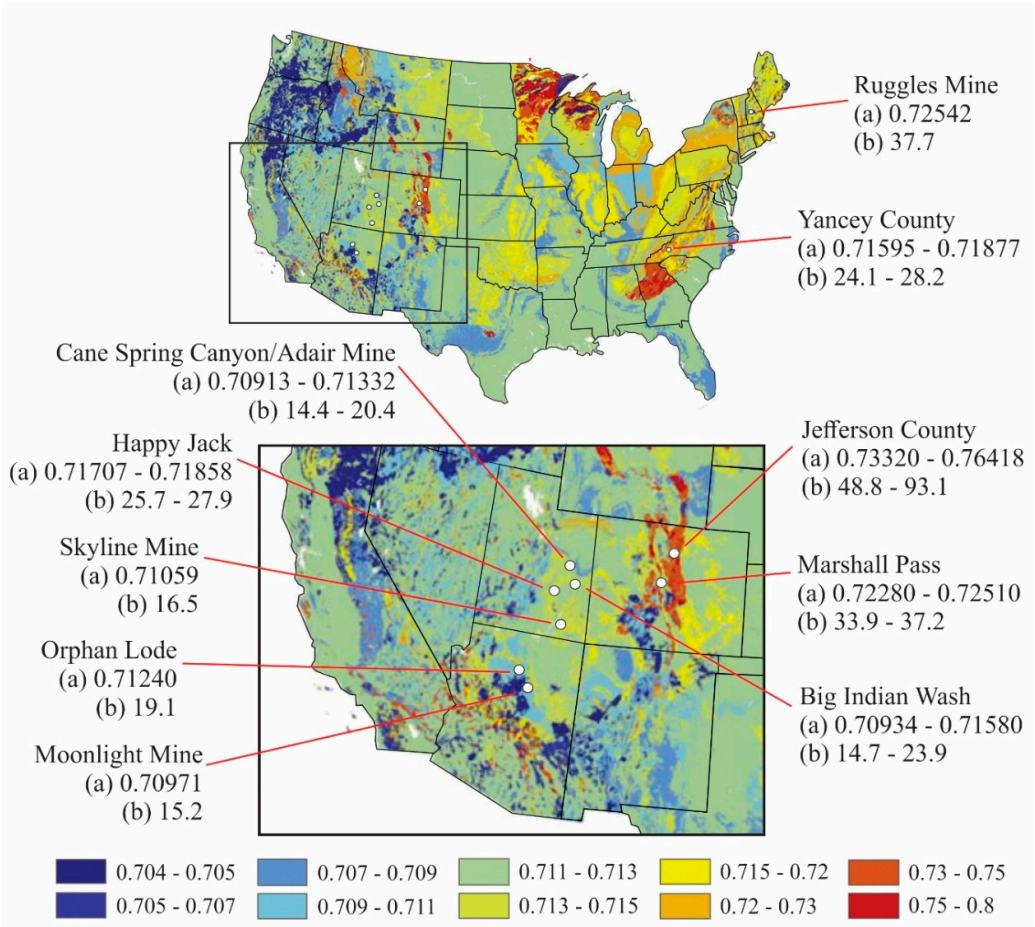

Figure 4. Initial $^{87}Sr/^{86}Sr$ (**a**) and ε_{Sr} values (**b**, as defined in text) of uraninite from this study and Corcoran et al. [59] overlain on $^{87}Sr/^{86}Sr$ isoscape map for continental U.S. (from Bataille and Bowen [60]).

3.4. U Isotope Data

U isotope ratios for uraninite, investigated here, are listed in Table 5. For this study, the average external reproducibility (2σ level) associated with the $^{238}U/^{235}U$, $^{234}U/^{238}U$, and $^{235}U/^{238}U$ ratios are 0.3‰, 8.18‰, and 0.79‰, respectively. Figure 5 displays the $\delta^{238}U$ values for pristine solutions of uraninite,

obtained here, as compared with those from several previous analogous studies of uraninite (Table S1).

The $\delta^{238}U$ values for uraninite from a deposit type yield a range of values that are either all negative or all positive (not mixed) with the exception of those from metamorphite polymetallic, sandstone, and Proterozoic unconformity contact deposits (Figure 5). Granite-related deposits were separated into two subtypes; deposits of an endogranitic nature yield negative $\delta^{238}U$ values, whereas perigranitic uraninite are characterized by positive values (Figure 5).

Secular equilibrium is affected by fluid–mineral interaction either by post depositional alteration, or chemical weathering induced leaching [24]. Negative $\delta^{234}U$ values indicate the loss of U, whereas positive $\delta^{234}U$ values are associated with U gain. The majority (69%) of $\delta^{234}U$ values, determined here, are between −10‰ and +10‰. Proterozoic unconformity basement-related uraninite is the only type with $\delta^{234}U$ values greater than +10 (Table 5 and S1).

Figure 6 illustrates an overall positive trend between $^{207}Pb/^{206}Pb$ and $^{238}U/^{235}U$ ratios for uraninite examined in this study. Great Bear uraninite is characterized by the lowest $^{238}U/^{235}U$ at 137.56. A positive array is observed when $^{207}Pb/^{206}Pb$ ratios are plotted against initial $^{87}Sr/^{86}Sr$ values (Figure 6b). Figure 6c displays Ba/Sr ratios (log scale) versus initial $^{87}Sr/^{86}Sr$ values and the result is also an overall positive trend.

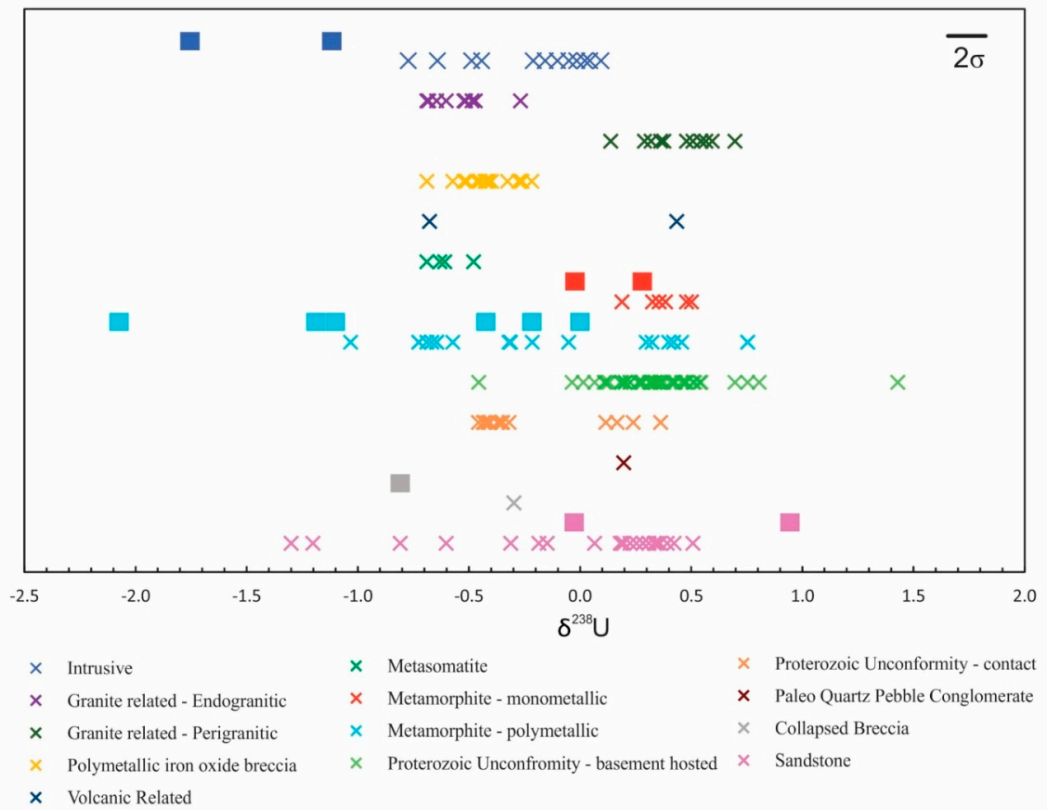

Figure 5. Natural $^{238}U/^{235}U$ ratios of uraninite plotted as $\delta^{238}U$ (defined in text) based on their deposit type. Uraninites from this study (solid squares) and several other previous studies (X symbols), which include: [9,20,25,50,51,59,61,62]. Solid line in upper right corner represents external reproducibility.

4. Discussion

A large concentration of uranium deposits are located within the western USA [63]. This presumably results from the prolonged tectonic activity in the area, such as the Laramide orogeny, which occurred between 80 and 35 million years ago [64], although it is most likely not the only factor. Such regional tectonic events could have had a significant impact on the geochemistry and isotopic signatures associated with uraninite mineralization.

Figure 1a–d indicates that trace element abundances and their incorporation within uraninite is controlled primarily by the crystal structure, and these display some fractionation relative to canonical values for continental crust [52] and sediments [53,54]. Detailed examination of trace elemental ratios for pristine and corresponding altered sections for the same uraninite sample indicate higher La/Yb ratios for the latter (Figure 1a and Table 2). If the La/Yb ratio serves as a proxy for monitoring the degree of light vs. heavy rare earth elements (LREE/HREE) enrichment, then the results shown in Figure 1a suggest the larger LREEs are preferentially incorporated into uraninite alteration products. The latter feature has also been documented in a recent study by Balboni et al. [29]. Figure 1b,d indicates greater variation for Nb abundances relative to the other trace elements depicted in Figure 1 as the former span >4 orders of magnitude. In general, Figure 1d displays the removal of the more mobile elements Ta and Nb from pristine uraninite into altered sections, which is facilitated by the similar ionic radii of Y and Yb with that of uranium. Moreover, the mobility of Ta and Nb is dependent on the chemistry of the fluid/melt, and in turn the degree of interaction between the host rock and corresponding source rock [6]. The higher and more variable Zr/Hf ratios as compared with Rb/Cs values (Figure 1c) is not a crystallographic-controlled feature but is rather a source-dominated result. For example, sample 625 is from a sandstone-type deposit (Moonlight Mine) and thus its high Zr/Hf ratio could reflect the presence of detrital zircon in the precursor host rock. The remaining uraninite samples with high Zr/Hf values could simply reflect regional host rock source compositions or the result of U ore formation processes, such as metamorphism (e.g., Great Bear). The high Rb/Cs ratio for the altered Billiken sample could be attributed to contamination by K-feldspar from the host rock (Figure 1c). Figure 1a illustrates that initial $^{87}Sr/^{86}Sr$ values are age dependent, i.e., older metamorphite uraninites is characterized by higher initial Sr values, whereas much younger pegmatitic uraninite plot at lower ratios; intermediate initial Sr isotope values are recorded by uraninite aged between ~44 and 440 Ma. This interpretation is consistent with that postulated by [65].

Figure 6a plots $^{238}U/^{235}U$ vs. $^{207}Pb/^{206}Pb$ ratios for the uraninite samples, investigated here, and the latter value reflects a combined contribution from both common and radiogenic Pb sources; increased contributions from both components result in higher $^{207}Pb/^{206}Pb$ ratios since older deposits contain more radiogenic Pb. However, there does not seem to be a definitive temporal variation in the $^{238}U/^{235}U$ ratios (Figure 6a). The Great Bear uraninite is the oldest sample in this study and has the lowest $^{238}U/^{235}U$ ratio, which is attributed to vastly different paleo environmental conditions (e.g., oxidation state [19]) at the time of mineralization (Figure 6a). Figure 6b displays an overall positive trend between initial $^{87}Sr/^{86}Sr$ and $^{207}Pb/^{206}Pb$, which could be attributed to radiogenic in-growth over time; i.e., samples with higher initial ratios for both isotope systems are older. Moreover, the overall positive correlation between Ba/Sr and initial $^{87}Sr/^{86}Sr$ ratios could be attributed to the increasing involvement of K-feldspar, which preferentially incorporates both Ba and Rb within the host crust (Figure 6c). For example, K-feldspar is an abundant mineral in high pressure and temperature metamorphic terrains, such as the one hosting the Great Bear uraninite deposit. The results, presented here, indicate that despite the complex chemical nature of uraninite and its capacity to incorporate a variety of trace elements, it is nonetheless still possible to identify specific deposit locations that occur within proximity of each other (e.g., <300 km apart in southwestern USA) due to their contrasting isotope signatures (Figures 1, 3, and 6).

Accurate and rapid assessment of forensic signatures for intercepted illicit nuclear material requires reliable, proven, and state-of-the-art analytical techniques. Traditional isotopic measurements are conducted using acid digestion followed by ion exchange chromatography, which can take weeks to complete [17]. Recent advances in MC-ICP-MS instrumentation combined with laser ablation technology have provided the ability to obtain accurate chemical (e.g., [51]) and isotopic results within days (e.g., [66]).

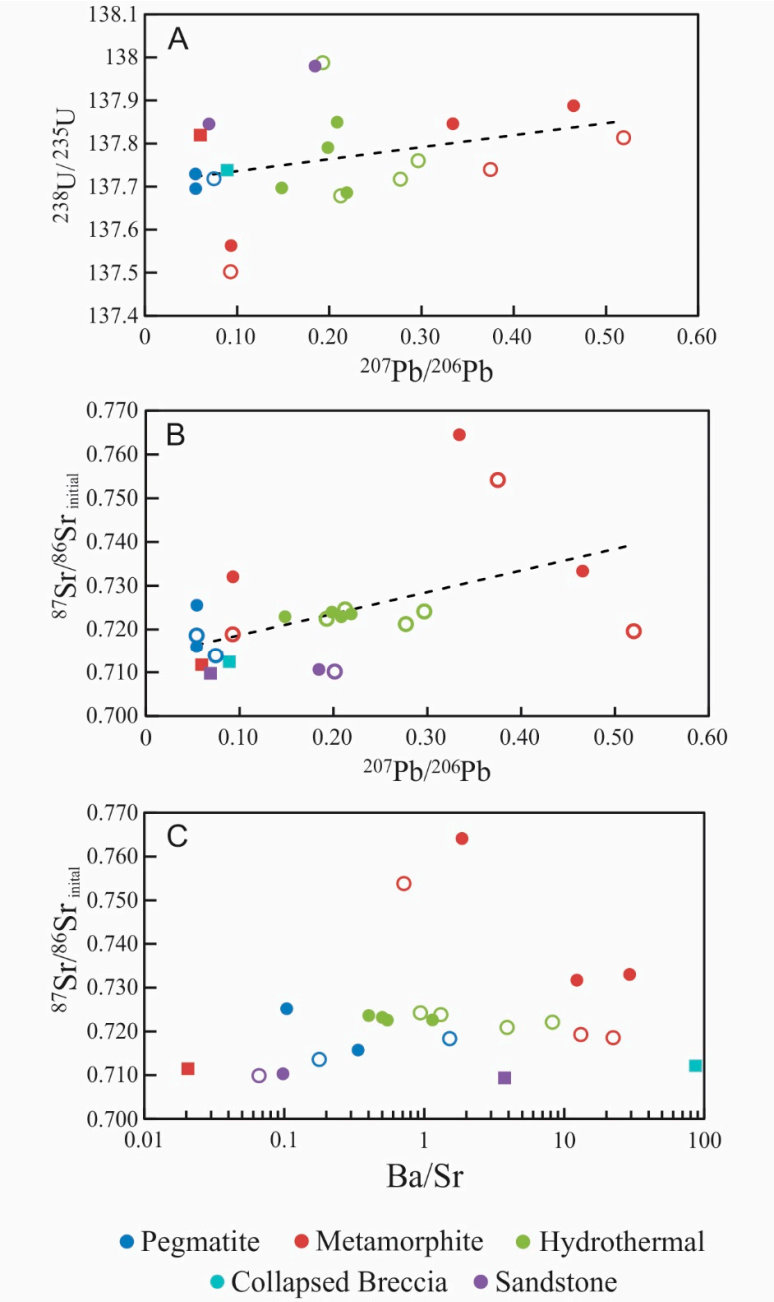

Figure 6. Isotopic and Ba/Sr signatures of uraninite from several deposit types. (**A**) $^{207}Pb/^{206}Pb$ vs. $^{238}U/^{235}U$; (**B**) $^{207}Pb/^{206}Pb$ vs. $^{87}Sr/^{86}Sr$; (**C**) Ba/Sr vs. $^{87}Sr/^{86}Sr$ (A–C). Solid circles denote pristine sample, open circles represent altered fraction, and square symbols represent bulk samples where pristine and altered aliquots could not be separated.

The secondary Pb-Pb isochron ages, obtained here, by both SM- and LA-MC-ICP-MS are in general within good agreement of one another, and with previously documented ages for these same U ore deposits (Figures 2 and S1). Hence, these results support the use of the LA-MC-ICP-MS method for common Pb age dating of uraninite as a viable nuclear forensic tool. Isotopic measurements conducted using SM-MC-ICP-MS are associated with much lower uncertainties as compared with those obtained by LA-MC-ICP-MS. In general, laser ablation analyses are associated with a higher uncertainty because, unlike solution mode analyses, the elements of interest are not separated from the U-rich matrix and the laser ablation ion signals are transient in nature; i.e., are not stable and decrease as a function of time of analysis. For Shinkolobwe, the uraninite matrix appeared to be

"softer" as compared with the remaining uraninite samples, which influenced and reduced the efficiency of the ablation process. Marshall Pass samples were heavily altered throughout, which could have affected the ablation process via the presence of micro fractures within the uraninite resulting in higher uncertainties (i.e., less stable ion signals). Nevertheless, the LA-MC-ICP-MS analyses provide valuable information on the relative ages of uraninites, being investigated, i.e., whether it is billions of years old, or formed within the last 100 million years. In a nuclear forensic analysis, this type of information will prove useful in constraining the possible U deposits of origin.

Lewis et al. [67] showed that uraninite could be texturally and compositionally heterogeneous at the micron scale. Application of the LA-MC-ICP-MS method provides spatially resolved ages for both the mineralization and the associated alteration of uraninite, which can both be easily masked by bulk sample analysis by SM-MC-ICP-MS. Analyses conducted using LA-MC-ICP-MS have the capability to specifically target regions of interest on a sample at the 10 to 100 s of micron scale and hence avoid potential contamination from mineral inclusions and host rock materials. Uraninites from Jefferson, Billiken, and Shinkolobwe are the only three samples that did not give reliable ages. Ages determined for the uraninite from Billiken Lode of 537 ± 37 and 733 ± 1200 Ma do not match the previously documented age of 69.3 ± 1.1 Ma; this discrepancy can be explained by possible contamination from the host rock (Proterozoic age). This is supported by further examination of the LA-MC-ICP-MS analyses, since two separate secondary Pb-Pb isochrons associated with lower uncertainties yield a younger (476 ± 110 Ma) and older (1255 ± 65 Ma) age, the latter result is closer in age to that of the host rock for the Billiken uraninite sample (Figure S1).

Isotopic measurements of both digested pristine and altered uraninite fragments were used to generate two-point secondary Pb-Pb isochrons for SM-MC-ICP-MS analyses. The agreement between ages, obtained here, with those previously documented for uraninite indicates that the alteration event occurred soon after the time of mineralization. Evidence for more recent alteration events is also corroborated by the negative $\delta^{234}U$ values (Table 5), which can be attributed to uranium leaching [9]. Comparison between ages obtained by LA-MC-ICP-MS for the pristine (>80 wt% UO_2) and altered (<80 wt% UO_2) regions in Marshall 4 uraninite suggest the alteration occurred relatively soon after its crystallization (Figure 2). Marshall 3 yields the youngest age via SM-MC-ICP-MS; however, the LA-MC-ICP-MS results for this same sample has pristine uraninite yielding an age of 145 ± 240 Ma and altered areas give −122 ± 55 Ma. Thus, the latter result obtained by SM-MC-ICP-MS for Marshall 3 reflects a very recent alteration event, which is supported by the $\delta^{234}U$value of −64.69. On the basis of the ages obtained in this study of 1509 ± 19 and 1444 ± 61 Ma by SM- and LA-MC-ICP-MS, respectively, the uraninite from Great Bear is further confirmed to originate from the Echo Bay mine (1500 ± 10 to 1424 ± 29 Ma) within the Great Bear region.

The erroneous and negative Rb-Sr isochron ages indicate that the uraninite samples were affected by open system behavior most likely involving hydrothermal fluids. Rubidium has a much larger radius (1.48 Å) compared to both Sr (1.13 Å) and U (1.0 Å). Thus, this large difference in ionic radius can render Rb incompatible within the uraninite structure. In contrast, Sr can substitute for Ca (an important impurity) in eight-fold coordinated sites within UO_{2+x} making Sr more compatible. The different geochemical properties between Rb and Sr could cause a fractionation between the parent and daughter isotope during fluid interaction, which does not affect the Pb isotopes. Alteration events must have occurred during the last 2.5 Ma within the southwestern USA, as indicated by the range of negative $\delta^{234}U$ values from −2 to −65 (and up to +47), which could also have disturbed the Rb-Sr isotope systematics of uraninite. The elevated $^{87}Sr/^{86}Sr$ values, reported here, suggest that the source of Sr, similar to that for the U, is predominantly of crustal origin. This interpretation is corroborated by the fact that older Nd-model craton ages [21] are associated with higher initial $^{87}Sr/^{86}Sr$ (and εSr values) for uraninites, investigated here (Figure 3). The influence of the host rock on uraninite mineralization is further emphasized by the correlation between higher predicted $^{87}Sr/^{86}Sr$ values based on isoscape maps for the continental USA [60] and higher Sr values, reported here (Figure 4).

Several recent studies have investigated the main mechanism behind U isotope fractionation. Figure 5 illustrates the U isotope fractionation associated with several types of U deposits. Higher

$\delta^{238}U$ values are preferred within the lower oxidation state as per the nuclear field shift [9]. Although U isotope fractionation is dominated by reduction of U, the oxidation state is overprinted by increasing temperature [24]; as the temperature increases, the degree of isotopic fractionation decreases [9]. However, pegmatitic-type U ore deposits within the Appalachian mountain belt (Ruggles and Yancey) display lower $\delta^{238}U$ values than previously documented [9], as low as −1.76 (Figure 5). These negative $\delta^{238}U$ values indicate that although temperature plays an important role during uraninite formation, it is not the sole mechanism responsible for U fractionation. Similar to the results from Uvarova et al. [9], U deposits associated with lower ore grades tend to have more negative $\delta^{238}U$ values than those associated with higher ore grades (Figure 5). Metamorphite and sandstone uranium deposits share similar mechanisms for ore formation with continual remobilization and crystallization of uraninite. The latter could be responsible for the highly variable $\delta^{238}U$ values [62], shown in Figure 5. The range of $\delta^{238}U$ values can also be related to the degree of U leaching from the host rock [24], which is linked to fluid interaction and the preferential removal of weakly bound ^{234}U. However, careful examination of all the data, reported here, indicates that there is no correlation between $\delta^{238}U$ and $\delta^{234}U$ values (Figure S3).

5. Conclusions

Ages obtained for uraninite based on secondary Pb-Pb isochrons are in good agreement with those reported in the literature for the U ore deposits investigated here. Moreover, age results obtained by SM-MC-ICP-MS corroborate those determined by LA-MC-ICP-MS. The latter method provides spatially resolved age information for mineralization and alteration of uraninite in a shorter period of time as compared with conventional dating methods (e.g., ID-TIMS). LA-MC-ICP-MS measurements are associated with higher uncertainties as compared with those obtained by SM-MC-ICP-MS; however, useful age information can still be obtained from the former, i.e., clearly distinguish between uraninites that are characterized by vastly distinct ages. The trace element concentrations for uraninite indicate that the crystal structure dictates the incorporation of impurities followed by element availability. The large ionic radius of Rb (in particular relative to U and Pb) renders it more mobile during secondary alteration (open system) processes, consequently, eliminating the effectiveness of the Rb-Sr geochronometer for age determination of uraninite. Initial $^{87}Sr/^{86}Sr$ ratios for uraninite samples, investigated here, are in general positively correlated with the age of the host craton, i.e., higher initial $^{87}Sr/^{86}Sr$ values are found within older cratons. The U isotope signatures determined for uraninite, examined here, further support the variety of processes responsible for isotope fractionation, and these include temperature, the nuclear field effect, oxidation, and source rock composition.

Supplementary Materials: The following are available online at www.mdpi.com/xxx/s1, Figure S1: Secondary Pb-Pb isochrons determined using SM- and LA-MC-ICP-MS for uraninites from this study, Figure S2: Rb-Sr isochrons obtained by SM-MC-ICP-MS. All ellipses are at the 2σ level for uncertainty, Figure S3: $\delta^{238}U$ and $\delta^{234}U$ values, Table S1: Complied list of uraninites from several previous studies.

Author Contributions: Conceptualization, A.S. and S.L.; funding acquisition, A.S.; investigation, S.L, L.C., and S.S.; methodology, A.S., S.S., and C.D.; resources, P.B.; writing—original draft preparation, S.L. and A.S.; writing—review and editing, S.L., A.S., L.C., S.S., C.D., and P.B. All authors have read and agreed to the published version of the manuscript.

Funding: This research was funded by the United States Department of Homeland Security, grant number 2014-DN-077-ARI082.

Acknowledgments: The authors thank Ian Steele for his assistance and expertise with operation of the EMP and Notre Dame's Center of Environmental Science and Technology (CEST) for use of the μ-XRF.

Conflicts of Interest: The authors declare no conflict of interest. The funders had no role in the design of the study; in the collection, analyses, or interpretation of data; in the writing of the manuscript, or in the decision to publish the results.

References

1. Hore-Lacy, I. *Uranium for Nuclear Power: Resources, Mining and Transformation to Fuel*; Woodhead Publishing: Cambridge, UK, 2016.
2. IAEA. Geological Classification of Uranium Deposits and Description of Selected Examples; IAEA-TECDOC-1842; IAEA: Vienna, Austria, 2018; pp. 1–430.
3. Janeczek, J.; Ewing, R.C. Structural formula of uraninite. *J. Nucl. Mater.* **1992**, *190*, 128–132.
4. Moody, K.J.; Hutcheon, I.D.; Grant, P.M. *Nuclear Forensic Analysis*; Taylor and Francis Group: Abingdon, UK, 2005.
5. Mercadier, J.; Cuney, M.; Lach, P.; Boiron, M.; Bonhoure, J.; Richard, A.; Leisen, M.; Kister, P. Origin of uranium deposits revealed by their rare earth element signature. *Terra Nova* **2011**, *23*, 264–269, doi:10.1111/j.1365-3121.2011.01008.x.
6. Frimmel, H.E.; Schedel, S.; Brätz, H. Uraninite chemistry as forensic tool for provenance analysis. *Appl. Geochem.* **2014**, *48*, 104–121, doi:10.1016/j.apgeochem.2014.07.013
7. Bellucci, J.J.; Simonetti, A.; Koeman, E.C.; Wallace, C.; Burns, P.C. A detailed geochemical investigation of post-nuclear detonation trinitite glass at high spatial resolution: Delineating anthropogenic vs. natural components. *Chem. Geol.* **2014**, *365*, 69–86, doi:10.1016/j.chemgeo.2013.12.001.
8. Dustin, M.K.; Koeman, E.C.; Simonetti, A.; Torrano, Z.; Burns, P.C. Comparative investigation between in situ laser ablation versus bulk sample (solution mode) inductively coupled plasma mass spectrometry (ICP-MS) analysis of trinitite post-detonation materials. *Appl. Spectrosc.* **2016**, *70*, 1446–1455.
9. Uvarova, Y.A.; Kyser, T.K.; Geagea, M.L.; Chipley, D. Variations in the uranium isotopic compositions of uranium ores from different types of uranium deposits. *Geochim. Cosmochim. Acta* **2014**, *146*, 1–17, doi:10.1016/j.gca.2014.09.034.
10. Martz, P.; Mercadier, J.; Perret, J.; Villeneuve, J.; Deloule, E.; Cathelineau, M.; Quirt, D.; Doney, A.; Ledru, P. Post-crystalliztion alteration of natural uraninites: Implications for dating, tracing, and nuclear forensics. *Geochim. Cosmochim. Acta* **2019**, *249*, 138–159, doi:10.1016/j.gca.2019.01.025.
11. Cross, A.; Jaireth, S.; Rapp, R.; Armstrong, R. Reconnaissance-style EPMA chemical U–Th–Pb dating of uraninite. *Aust. J. Earth Sci.* **2011**, *58*, 675–683, doi:10.1080/08120099.2011.598190.
12. Finger, F.; Waitzinger, M.; Förster, H.J.; Kozlik Raith, J.G. Identification of discrete low-temperature thermal events in polymetamorphic basement rocks using high spatial resolution FE-SEM-EDX U-Th-Pb dating of uraninite microcrystals. *Geology* **2017**, *45*, 991–994.
13. Zong, K.Q.; Chen, J.Y.; Hu, Z.C.; Liu, Y.S.; Li, M.; Fan, H.H.; Meng, Y.N. Insitu U-Pb dating of uraninite by fs-LA-ICP-MS. *Sci. China Earth Sci.* **2015**, *58*, 1731–1740, doi:10.1007/s11430-015-5154-y.
14. Shabaga, B.M.; Fayek, M.; Quirt, D.; Jefferson, C.W.; Camacho, A. Mineralogy, geochronology, and genesis of the Andrew Lake uranium deposit, Thelon Basin, Nunavut, Canada. *Can. J. Earth Sci.* **2017**, *54*, 850–868.
15. Amelin, Y.; Kaltenbach, A.; Iizuka, T.; Stirling, C.H.; Ireland, T.R.; Petaev, M.; Jacobsen, S.B. U–Pb chronology of the Solar System's oldest solids with variable $^{238}U/^{235}U$. *Earth Planet. Sci. Lett.* **2010**, *300*, 343–350, doi:10.1016/j.epsl.2010.10.015.
16. Corcoran, L.; Simonetti, A. Geochronology of uraninite revisited. *Minerals* **2020**, in press.
17. Hutcheon, I.D.; Kristo, M.J.; Knight, K.B. Nonproliferation nuclear forensics. In *Uranium: From Cradle to Grave*; Burns, P.C., Sigmon, G.E., Eds.; Mineralogical Association of Canada: Québec, QC, Canada, 2013; Volume 43, pp. 15–119.
18. Alves, A.; de Assis Janasi, V.; Simonetti, A.; Heaman, L. Microgranitic enclaves as products of self-mixing events: a study of open-system processes in the Mauá Granite, São Paulo, Brazil, based on in situ isotopic and trace elements in plagioclase. *J. Petrol.* **2009**, *50*, 2221–2247, doi:10.1093/petrology/egp074.
19. Cuney, M. Evolution of uranium fractionation processes through time: Driving the secular variation of uranium deposit types. *Econ. Geol.* **2010**, *105*, 553–569.
20. Kirchenbaur, M.; Maas, R.; Ehrig, K.; Kamenetsky, V.S.; Strub, E.; Ballhaus, C.; Münker, C. Uranium and Sm isotope studies of the supergiant Olympic Dam Cu–Au–U–Ag deposit, South Australia. *Geochim. Cosmochim. Acta* **2016**, *180*, 15–32, doi:10.1016/j.gca.2016.01.035.
21. Bennett, V.C.; DePaolo, D.J. Proterozoic crustal history of the western United States as determined by neodymium isotopic mapping. *Geol. Soc. Am. Bull.* **1987**, *99*, 674–685.
22. Varga, Z.; Wallenius, M.; Mayer, K.; Keegan, E.; Millet, S. Application of lead and strontium isotope ratioe measurements for the origin assessment of uranium ore concentrates. *Anal. Chem.* **2009**, *81*, 8327–8334.

23. Yang, S.; Liu, Y. Nuclear field shift effects on stable isotope fractionation: a review. *Acta Geochim.* **2016**, *35*, 227–239, doi:10.1007/s11631-016-0109-3.
24. Andersen, M.B.; Stirling, C.H.; Weyer, S. Uranium isotope fractionation. *Miner. Geochem.* **2017**, *82*, 799–850.
25. Bopp, C.J., IV; Lundstrom, C.C.; Johnson, T.M.; Glessner, J.J.G. Variations in $^{238}U/^{235}U$ in uranium ore deposits: Isotopic signatures of the U reduction process? *Geology* **2009**, *37*, 611–614, doi:10.1130/G25550A.1.
26. Brennecka, G.A.; Borg, L.E.; Hutcheon, I.D.; Sharp, M.A.; Anbar, A.D. Natural variations in uranium isotope ratios of uranium ore concentrates: Understanding the $^{238}U/^{235}U$ fractionation mechanism. *Earth Planet. Sci. Lett.* **2010**, *291*, 228–233, doi:10.1016/j.epsl.2010.01.023.
27. Balboni, E.; Jones, N.; Spano, T.; Simonetti, A.; Burns, P.C. Chemical and Sr isotopic characterization of North America uranium ores: Nuclear forensic applications. *Appl. Geochem.* **2016**, *74*, 24–32.
28. Balboni, E.; Simonetti, A.; Spano, T.; Cook, N.; Burns, P.C. Rare-earth element fractionation in uranium ore and its U(VI) alteration. *Appl. Geochem.* **2017**, *87*, 84–92, doi:10.1016/j.apgochem.2017.10.007.
29. Brobst, D.A. *Geology of the Spruce Pine District Avery, Mitchell, and Yancey Counties North Carolina*; Bulletin 1122-A; U.S. Geological Survey: Reston, VA, USA, 1962.
30. Shaub, B.M. The occurrence, crystal habit and composition of the uraninite from the Ruggles Mine, near Grafton Center, New Hampshire. *Am. Miner.* **1938**, *23*, 334–341.
31. Olson, J.C. *Mica-bearing Pegmatites of New Hampshire*; Geological Survey Bulletin; US Government Printing Office: Washington, DC, USA, 1941.
32. Korzeb, S.L.; Foord, E.E.; Lichte, F.E. The chemical evolution and paragenesis of uranium minerals from the Ruggles and Palermo Granitic Pegmatites, New Hampshire. *Can. Miner.* **1997**, *35*, 135–144.
33. Miller, R.G. The geochronology of uranium deposits in the Great Bear batholith, Northwest Territories. *Can. J. Earth Sci.* **1982**, *19*, 1428–1448.
34. Decrée, S.; Deloule, É.; De Putter, T.; Dewaele, S.; Mees, F.; Yans, J.; Marignac, C. SIMS U-Pb dating of uranium mineralization in the Katanga Copperbelt: Constraints for the geodynamic context. *Ore Geol. Rev.* **2011**, *40*, 81–89, doi:10.1016/j.oregeorev.2011.05.003
35. Dahlkamp, F.J. *Uranium Ore Deposits*; Springer: Berlin/Heidelberg, Germany; New York, NY, USA, 1991.
36. Zhao, D.; Ewing, R.C. Alteration products of uraninite from the Colorado Plateau. *Radiochim. Acta* **2000**, *88*, 739–749.
37. Deditius, A.P.; Utsunomiya, S.; Ewing, R.C. Fate of trace elements during alteration of uraninite in a hydrothermal vein-type U-deposit from Marshall Pass, Colorado, USA. *Geochim. Cosmochim. Actata* **2007**, *71*, 4954–4973.
38. Granger, H.C.; Raup, R.B. *Reconnaissance Study of Uranium Deposits in Arizona*; Geological Survey Bulletin; US Government Printing Office: Washington, DC, USA, 1962.
39. Burns, P.C.; Finch, R. *Uranium: Mineralogy, Geochemistry and the Environment*; Mineralogical Society of America: Washington, DC, USA, 1999.
40. Johnson, H.S.; Thordarson, W. *Uranium deposits of the Moab, Monticello, White Canyon and Monument Valley districts Utah and Arizona*; Geological Survey Bulletin; US Government Printing Office: Washington, DC, USA, 1966.
41. Fayek, M. Uranium Ore Deposits—A Review. In *Uranium: From Cradle to Grave*; Burns, P.C., Sigmon, G.E., Eds.; Mineralogical Association of Canada: Québec, QC, Canada, 2013; Volume 43, pp. 121–146.
42. Schmidberger, S.S.; Simonetti, A.; Heaman, L.M.; Creaser, R.A.; Whiteford, S. Lu–Hf, in-situ Sr and Pb isotope and trace element sustematics for mantle eclogites from the Diavik diamond mine: Evidence for Paleoproterozoic subduction beneath the Slave craton. *Can. Earth Planet. Sci Lett.* **2007**, *254*, 55–68.
43. Schurr, M.R.; Donohue, P.H.; Simonetti, A.; Dawson, E. Multi-element and lead isotope characterization of early nineteenth century pottery sherds from Native American and Euro-American sites. *J. Archaeol. Sci. Rep.* **2018**, *20*, 390–399.
44. Jenner, G.A.; Longerich, H.P.; Jackson, S.E.; Fryer, B.J. ICP-MS- A powerful tool for high-precision trace-element analysis in Earth sciences: Evidence from analysis of selected U.S.G.S reference samples. *Chem. Geol.* **1990**, *83*, 133–48.
45. Manhes, G.; Minster, J.F.; Allègre, C.J. Comparative uranium-thorium-lead and rubidium-strontium study of the Saint Sèverin amphoterite: consequences for early solar system chronology. *Earth Planet. Sci. Lett.* **1978**, *39*, 14–24.

46. Simonetti, A.; Gariépy, C.; Banic, C.M.; Tanabe, R.; Wong, H.K. Pb isotopic investigation of aircraft-sampled emissions from the Horne smelter (Rouyn, Québec): Implications for atmospheric pollution in northeastern North America. *Geochim. Cosmochim. Acta* **2004**, *68*, 3285–3294.
47. Crock, J.G.; Lichte, F.E.; Wildeman, T.R. The group separation of the rare-earth elements and yttrium from geologic materials by cation-exchange chromatography. *Chem. Geol.* **1984**, *45*, 149–163.
48. Faure, G.; Mensing, T.M. *Isotopes: Principles and Applications*. Wiley-Blackwell: Hoboken, NJ, USA, 2005.
49. Martinelli, R.E.; Hamilton, T.F.; Williams, R.W.; Kehl, R.W. Separation of uranium and plutonium isotopes for measurement by multi collector inductively coupled plasma mass spectroscopy. *J. Radioanal. Nucl. Chem.* **2009**, *282*, 343–347, doi:10.1007/s10967-009-0150-3.
50. Cheng, H.; Edwards, R.L.; Shen, C.C.; Polyak, V.J.; Asmerom, Y.; Woodhead, J.; Hellstrom, J.; Wang, Y.; Kong, X.; Spötl, C.; et al. Improvements in ^{230}Th dating, ^{230}Th and ^{234}U half-life values, and U–Th isotopic measurements by multi-collector inductively coupled plasma mass spectrometry. *Earth Planet. Sci. Lett.* **2013**, *371*, 82–91, doi:10.1016/j.epsl.2013.04.006.
51. Spano, T.L.; Simonetti, A.; Balboni, E.; Dorais, C.; Burns, P.C. Trace element and U isotope analysis of uraninite and ore concentrate: Applications for nuclear forensic investigations. *Appl. Geochem.* **2017**, *84*, 277–285, doi:10.1016/j.apgeochem.2017.07.003.
52. Rudnick, R.L.; Gao, S. Composition of the continental crust. In *The Crust*; Rudnick, R.L., Ed.; Volume 3 Treatise on Geochemistry; Elsvier-Pergamon: Oxford, UK, 2005.
53. McLennan, S.M. Relationships between the trace element composition of sedimentary rocks and upper continental crust. *Geochem. Geophy. Geosys.* **2001**, *2*, doi:10.1029/2000GC000109.
54. Gromet, L.P.; Dymek, R.F.; Haskin, L.A.; Korotev, R.L. The "North American shale composite": Its compilation, major and trace element characteristics. *Geochim. Cosmochim. Acta* **1984**, *48*, 2469–2482.
55. Ludwig, K.R. *Isoplot 4.0: A Geochronological Toolkit for Microsoft Excel*; Berkeley Geochronology Center Special Publication: Berkeley, CA, USA, 2008.
56. Balboni, E. (University of Notre Dame, Notre Dame, IN, USA). Personal communications, 2018.
57. Ludwig, K.R.; Wallace, A.R.; Simmons, K.R. The Schwartzwalder Uranium Deposit, II: Age of Uranium Mineralization and Lead Isotope Constraints on Genesis. *Econ. Geol.* **1985**, *80*, 1858–1871.
58. Meneghel, L. The Occurrence of Uranium in the Katanga System of Northwestern Zambia. *Econ. Geol*. **1981**, *76*, 56–68.
59. Corcoran, L.; Simonetti, A.; Spano, T.L.; Lewis, S.R.; Dorais, C.; Simonetti, S.; Burns, P.C. Multivariant analysis of geochemical composition of uranium-rich samples. *Minerals* **2019**, *9*, 537, doi:10.3390/min9090537.
60. Bataille, C.P.; Bowen, G.J. Mapping 87Sr/86Sr variations in bedrock and water for large scale provenance studies. *Geochem. Geol.* **2012**, *304*, 39–52.
61. Hiess, J.; Condon, D.; McLean, N.; Noble, S. ^{238}U/^{235}U Systemics in terrestrial uranium-bearing minerals. *Science* **2012**, *335*, 1610–1614.
62. Chernyshev, I.V.; Golubev, V.N.; Chugaev, A.V.; Baranova, A.N. ^{238}U/^{235}U isotope ratio variations in minerals from hydrothermal uranium deposits. *Geochem. Int.* **2014**, *52*, 1013–1029, doi:10.1134/S0016702914120027.
63. Berge Exploration Inc. *United States Uranium Resource Map*; Berge Exploration: Denver, CO, USA, 1978. Available online: https://www.loc.gov/item/79692715/ (accessed on 6 December, 2019).
64. Livaccari, R. Role of crustal thickening and extensional collapse in the tectonic evolution of the Sevier-Laramide orogeny, western United States. *Geology* **1991**, *19*, 1104–1107.
65. Robb, L. *Introduction to Ore-Forming Processes*; Blackwell Publishing: Hoboken, NJ, USA, 2005.
66. Krachler, M.; Varga, Z.; Nicholl, A.; Wallenius, M.; Mayer, K. Spatial distribution of uranium isotopes in solid nuclear materials using laser ablation multi-collector ICP-MS. *Microchem. J.* **2018**, *140*, 24–30, doi:10.1016/j.microc.2018.03.038.
67. Lewis, S.R.; Simonetti, A.; Corcoran, L.; Spano, T.L.; Chung, B.W.; Teslich, N.E.; Burns, P.C. Characterization of uraninite using a FIB–SEM approach and its implications for LA–ICP–MS analyses. *J. Radioanal. Nucl. Chem.* **2018**, *318*, 1389–1400, doi:10.1007/s10967-018-6232-3.